

**IN THIS ISSUE**

Using Ultrasonic Extraction Method

Coffee Waste as a Recycled Resource

Drilled Piles in Collapsible Tropical

Usage of Wireless Intelligent Control



Great Britain  
Journals Press



IMAGE: OBSERVATORY WITH STAR TRAILS ON MOUNTAINS FOR CLEAR SKY

[www.journalspress.com](http://www.journalspress.com)

**LONDON JOURNAL OF  
ENGINEERING RESEARCH**

Volume 23 | Issue 5 | Compilation 1.0

Print ISSN: 2631-8474  
Online ISSN: 2631-8482  
DOI: 10.17472/LJER





Great Britain  
Journals Press

London Journal of Engineering Research

Volume 23 | Issue 5 | Compilation 1.0

## PUBLISHER

Great Britain Journals Press  
1210th, Waterside Dr, Opposite Arlington Building, Theale, Reading  
Phone: +444 0118 965 4033 Pin: RG7-4TY United Kingdom

## SUBSCRIPTION

*Frequency:* Quarterly

Print subscription

\$280USD for 1 year

\$500USD for 2 year

*(color copies including taxes and international shipping with TSA approved)*

Find more details at <https://journalspress.com/journals/subscription>

## ENVIRONMENT

Great Britain Journals Press is intended about Protecting the environment. This journal is printed using led free environmental friendly ink and acid-free papers that are 100% recyclable.

Copyright ©2023 by Great Britain Journals Press

All rights reserved. No part of this publication may be reproduced, distributed, or transmitted in any form or by any means, including photocopying, recording, or other electronic or mechanical methods, without the prior written permission of the publisher, except in the case of brief quotations embodied in critical reviews and certain other noncommercial uses permitted by copyright law. For permission requests, write to the publisher, addressed "Attention: Permissions Coordinator," at the address below. Great Britain Journals Press holds all the content copyright of this issue. Great Britain Journals Press does not hold any responsibility for any thought or content published in this journal; they belong to author's research solely. Visit <https://journalspress.com/journals/privacy-policy> to know more about our policies.

Great Britain Journals Press Headquarters

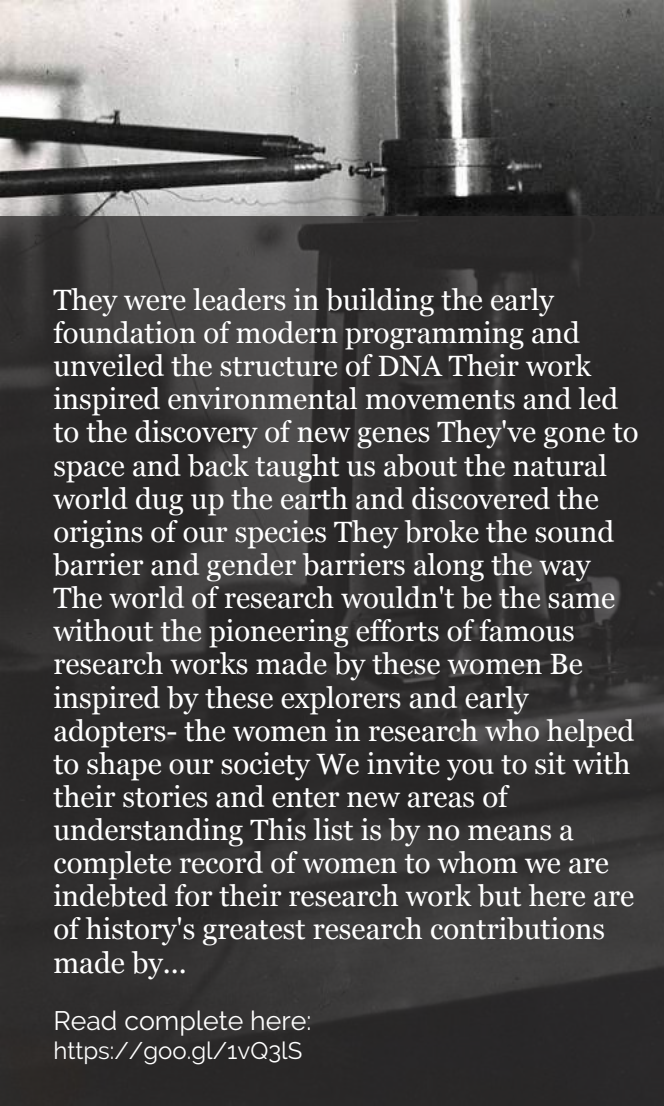
1210th, Waterside Dr,  
Opposite Arlington  
Building, Theale, Reading  
Phone: +444 0118 965 4033  
Pin: RG7-4TY  
United Kingdom

Reselling this copy is prohibited.

Available for purchase at [www.journalspress.com](http://www.journalspress.com) for \$50USD / £40GBP (tax and shipping included)

# Featured Blog Posts

blog.journalspress.com



They were leaders in building the early foundation of modern programming and unveiled the structure of DNA Their work inspired environmental movements and led to the discovery of new genes They've gone to space and back taught us about the natural world dug up the earth and discovered the origins of our species They broke the sound barrier and gender barriers along the way The world of research wouldn't be the same without the pioneering efforts of famous research works made by these women Be inspired by these explorers and early adopters- the women in research who helped to shape our society We invite you to sit with their stories and enter new areas of understanding This list is by no means a complete record of women to whom we are indebted for their research work but here are of history's greatest research contributions made by...

Read complete here:  
<https://goo.gl/1vQ3lS>

## Women In Research



## Computing in the cloud!

Cloud Computing is computing as a Service and not just as a Product Under Cloud Computing...

Read complete here:  
<https://goo.gl/VvHC7z>



## Writing great research...

Prepare yourself before you start Before you start writing your paper or you start reading other...

Read complete here:  
<https://goo.gl/np73jP>

# Journal Content

In this Issue



- i. Journal introduction and copyrights
  - ii. Featured blogs and online content
  - iii. Journal content
  - iv. Editorial Board Members
- 

- 1. Behavior of Laterally Top-Loaded Drilled Piles in Collapsible Tropical Soil. **1-9**
  - 2. Comparison of Thermal Numerical Simulation Data with Experimental Data from the ISCT 200-US Permanent Magnet Hall Thruster. **11-23**
  - 3. The Usage of Wireless Intelligent Control and UAV-Enabled B5G/6G Network in Fuzzy Adaptive Kalman Filter in INS/GNS Integrated Navigation System. **25-32**
  - 4. A Study on the Possibility of Utilizing Coffee Waste as a Recycled Resource Material using Ultrasonic Extraction Method. **33-40**
- 

- V. Great Britain Journals Press Membership

# Editorial Board

Curated board members



## Dr. Sharif H. Zein

School of Engineering,  
Faculty of Science and Engineering,  
University of Hull, UK Ph.D.,  
Chemical Engineering Universiti Sains Malaysia,  
Malaysia

## Prof. Hamdaoui Oualid

University of Annaba, Algeria Ph.D.,  
Environmental Engineering,  
University of Annaba,  
University of Savoie, France

## Prof. Wen Qin

Department of Mechanical Engineering,  
Research Associate, University of Saskatchewan,  
Canada Ph.D., Materials Science,  
Central South University, China

## Dr. Luisa Molari

Professor of Structural Mechanics Architecture,  
University of Bologna,  
Department of Civil Engineering, Chemical,  
Environmental and Materials, PhD in Structural  
Mechanics, University of Bologna.

## Prof. Chi-Min Shu

National Yunlin University of Science  
and Technology, Chinese Taipei Ph.D.,  
Department of Chemical Engineering University of  
Missouri-Rolla (UMR) USA

## Dr. Fawad Inam

Faculty of Engineering and Environment,  
Director of Mechanical Engineering,  
Northumbria University, Newcastle upon Tyne,  
UK, Ph.D., Queen Mary, University of London,  
London, UK

## Dr. Zoran Gajic

Department of Electrical Engineering,  
Rutgers University, New Jersey, USA  
Ph.D. Degrees Control Systems,  
Rutgers University, United States

## Prof. Te-Hua Fang

Department of Mechanical Engineering,  
National Kaohsiung University of Applied Sciences,  
Chinese Taipei Ph.D., Department of Mechanical  
Engineering, National Cheng Kung University,  
Chinese Taipei

### Dr. Rocío Maceiras

Associate Professor for Integrated Science,  
Defense University Center, Spain Ph.D., Chemical  
Engineering, University of Vigo, SPAIN

### Dr. Rolando Salgado Estrada

Assistant Professor,  
Faculty of Engineering, Campus of Veracruz,  
Civil Engineering Department, Ph.D.,  
Degree, University of Minho, Portugal

### Dr. Abbas Moustafa

Department of Civil Engineering,  
Associate Professor, Minia University, Egypt, Ph.D  
Earthquake Engineering and Structural Safety,  
Indian Institute of Science

### Dr. Wael Salah

Faculty of Engineering,  
Multimedia University Jalan Multimedia,  
Cyberjaya, Selangor, Malaysia, Ph.D, Electrical and  
Electronic Engineering, Power Electronics and Devices,  
University Sians Malaysia

### Prof. Baoping Cai

Associate Professor,  
China University of Petroleum,  
Ph.D Mechanical and Electronic Engineering,  
China

### Dr. Kao-Shing Hwang

Electrical Engineering Dept.,  
Nationalsun-Yat-sen University Ph.D.,  
Electrical Engineering and Computer Science,  
Taiwan

### Dr. Mu-Chun Su

Electronics Engineering,  
National Chiao Tung University, Taiwan,  
Ph.D. Degrees in Electrical Engineering,  
University of Maryland, College Park

### Nagy I. Elkalashy

Electrical Engineering Department,  
Faculty of Engineering,  
Minoufiya University, Egypt

### Dr. Vitoantonio Bevilacqua

Department of Electrical and Information  
Engineering Ph.D., Electrical Engineering  
Polytechnic of Bari, Italy

### Prof. Qingjun Liu

Professor, Zhejiang University, Ph.D.,  
Biomedical Engineering,  
Zhejiang University, China

Research papers and articles

Volume 23 | Issue 5 | Compilation 1.0





Scan to know paper details and  
author's profile

# Behavior of Laterally Top-Loaded Drilled Piles in Collapsible Tropical Soil

*Albuquerque, Paulo José Rocha & Carvalho, David*

*Universidade Estadual*

## ABSTRACT

Among the various types of loading to which foundations are subject, one can single out transversal (horizontal) forces. In general terms, we notice a lack of knowledge on the parameters used to design pile foundations with this type of load which will stress surface soil, considering that tropical soils are very often collapsible.

Aiming to furnish input for future geotechnical projects, transversal loading tests were performed on a bored pile and a continuous flight auger (CFA) pile, both 12.0 m in length, and 0.40 m in diameter. The loading tests were performed with the soil in its natural condition and by pre-flooding the area, at the UNICAMP (Universidade Estadual de Campinas) Experimental Soil Mechanics and Foundations Field I in Campinas/SP, Brazil, where the unsaturated soil is porous and classified as silty-sandy clay. The edometric tests indicated that is a collapsible soil in the surface bed up to 6.5m, and that the reduction in pre-collapse stress in the flooded condition is of the order of three times that of the natural condition. The load tests indicated that the maximum load in the natural condition is five times higher than in the flooded condition and that the value of  $n_h$  (horizontal reaction coefficient) reduces substantially with the effect of increasing soil moisture content.

*Classification:* LCC Code: TA775

*Language:* English



Great Britain  
Journals Press

LJP Copyright ID: 392921

Print ISSN: 2631-8474

Online ISSN: 2631-8482

London Journal of Engineering Research

Volume 23 | Issue 5 | Compilation 1.0



© 2023. Albuquerque, Paulo José Rocha & Carvalho, David. This is a research/review paper, distributed under the terms of the Creative Commons Attribution-Noncommercial 4.0 Unported License <http://creativecommons.org/licenses/by-nc/4.0/>, permitting all noncommercial use, distribution, and reproduction in any medium, provided the original work is properly cited.



# Behavior of Laterally Top-Loaded Drilled Piles in Collapsible Tropical Soil

Albuquerque, Paulo José Rocha<sup>α</sup> & Carvalho, David<sup>σ</sup>

## ABSTRACT

*Among the various types of loading to which foundations are subject, one can single out transversal (horizontal) forces. In general terms, we notice a lack of knowledge on the parameters used to design pile foundations with this type of load which will stress surface soil, considering that tropical soils are very often collapsible.*

*Aiming to furnish input for future geotechnical projects, transversal loading tests were performed on a bored pile and a continuous flight auger (CFA) pile, both 12.0 m in length, and 0.40 m in diameter. The loading tests were performed with the soil in its natural condition and by pre-flooding the area, at the UNICAMP (Universidade Estadual de Campinas) Experimental Soil Mechanics and Foundations Field I in Campinas/SP, Brazil, where the unsaturated soil is porous and classified as silty-sandy clay. The edometric tests indicated that is a collapsible soil in the surface bed up to 6.5m, and that the reduction in pre-collapse stress in the flooded condition is of the order of three times that of the natural condition. The load tests indicated that the maximum load in the natural condition is five times higher than in the flooded condition and that the value of  $n_h$  (horizontal reaction coefficient) reduces substantially with the effect of increasing soil moisture content.*

**Author α:** PhD, Full Professor, Universidade Estadual de Campinas - UNICAMP, FECFAU, Campinas/SP.

**σ:** PhD, Associate Professor, Universidade Estadual de Campinas - UNICAMP, Feagri, Campinas/ SP.

## I. INTRODUCTION

Horizontal load situations are frequent in foundations, but the technical community is largely unaware of the properties of collapsible

tropical soils when it comes to designing piles subjected to this effort (Albuquerque et al., 2019). This paper aims to fill part of the existing gap on this subject by obtaining valid parameters for the tropical collapsible soil common to the city of Campinas and other regions of Brazil, by carrying out horizontal load tests on drilled piles in the soil in the natural and flooded condition. This type of loading, in which the loading are often variable and cyclical, is also combined in some situations with tensile and compressive stresses.

Simplified mathematical models (Miche, 1930; Matlock and Reese, 1961; Broms, 1964; Poulos, 1971; Poulos and Davis 1980;) were created for analysis of transversal loads, since the modeling problems is three-dimensional and conventional solutions for project developers are extremely complex. The best-known and most widely used theory for evaluating these effects is the "horizontal reaction theory of soil", where the  $n_h$  factor represents the ratio between the reaction and displacement acting on the soil mass (Terzaghi, 1955; Palmer and Thompson, 1948; Davidson and Gill, 1963; Matlock and Reese, 1960, 1961; Davidson, 1970, Rosendo and Albuquerque, 2021; García et al, 2023). However, it is theoretically difficult to estimate this factor. However, it can be determined by load testing to obtain a reliable value for the transversal resistance of the construction soil.

The presence of collapsible soils is common in many regions of Brazil. Considering that these layers of collapsible soils can reach a depth of several meters and that the topsoil performs an important role in the behavior of transversely loaded piles, it is important to analyze the effect of this characteristic on the behavior of deep foundations. Analysis of the collapse potential is a very important factor to verify, as it most often dictates the behavior of unsaturated soils.

Collapsible soils are characterized by their high porosity and low degree of saturation and, through a process of increasing moisture content, suffer sudden and large additional deformations under constant total stresses.

Jennings and Knight (1957) provide a hypothesis for the phenomenon of collapse: the structure of a collapsible soil, when loaded at its natural moisture content, compresses smoothly, with no appreciable change in volume, resisting the compressive stresses between the grains, with no large relative movements between them. However, when this loaded soil gains moisture and reaches a critical moisture content, the bonds of resistance weaken and the structure collapses.

The grains or micro-aggregations are kept stable by the presence of suction (capillary and adsorption forces) and/or cementing agents (oxides, iron and/or aluminum hydroxides and carbonates). When these soils are moistened, these structure-stabilizing forces lose their intensity, allowing relative displacement between the particles, so that they begin to occupy the empty spaces in the soil structure (Dudley, 1970).

Thus, in order to provide parameters for the geotechnical environment, horizontal load tests were carried out at UNICAMP's Experimental Field of Soil Mechanics and Foundations I with natural and pre-flooded soil, with the aim of verifying the effect of collapsibility on the behavior of drilled piles (bored and CFA).

## II. GEOTECHNICAL AND GEOLOGICAL CHARACTERISTICS

This research was carried out at the Experimental Field for Soil Mechanics and Foundations I, located on the UNICAMP Campus (coordinates: -22.81937, -47.06047). Various in-situ and laboratory tests were carried out on disturbed and undisturbed samples. According to Carvalho et. al. (2000), the region's subsoil is formed by basic magmatites, with basic intrusive rocks from the Serra Geral Formation (diabase). They make up 98 km<sup>2</sup> of the Campinas region, occupying 14% of the total area. The profile of the Experimental Field is made up of diabase soil, with a surface

layer 6.5 m thick made up of high-porosity sandy-silty clay followed by a layer of sandy-clay silt up to 17 m. The water table level is found between 13 m and 16 m, depending on the time of year. It can be said that the first layer is made up of mature soil which has undergone an intense weathering process. The phenomenon of leaching may explain the porosity, due to the transport of fines to the deeper horizon. The second layer is formed by a young residual soil, which retains characteristics inherited from the original rock. Figure 1 shows the geotechnical profile obtained from the SPT and CPT tests and Table 2 shows the average parameters obtained from the laboratory tests.

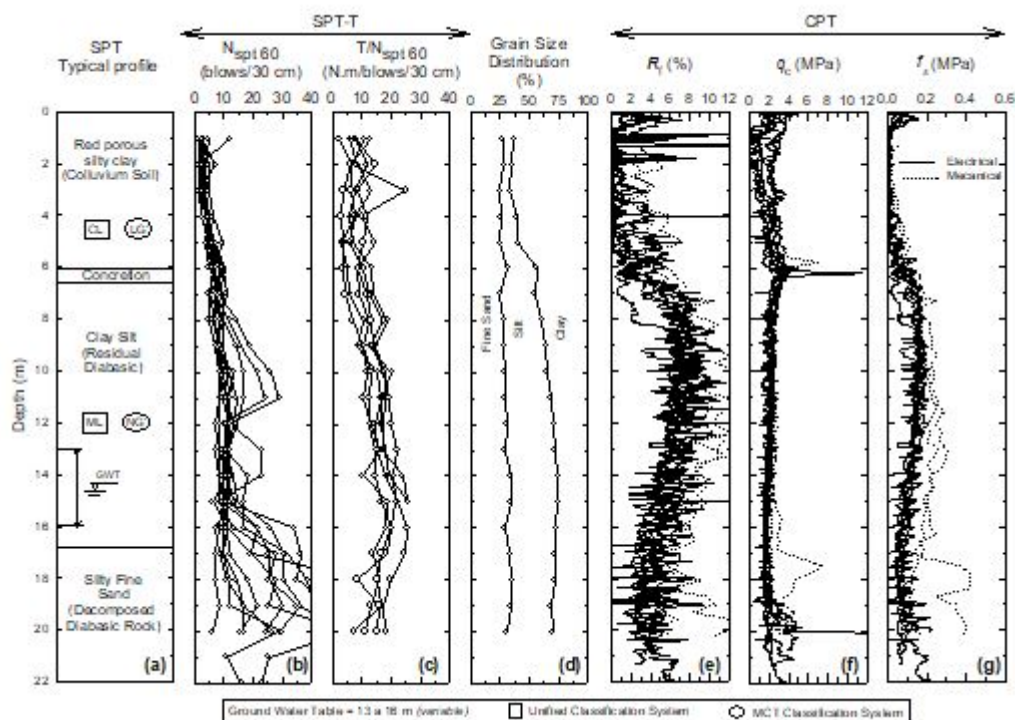


Figure 1: SPT-T and CPT (Electrical) Tests Results (Albuquerque et al, 2011)

Table 1: Average Physical Index Values

Layer	w (%)	e	n (%)	S <sub>r</sub> (%)
0 → 6.5m	23.8	1.72	63.1	41.4
6.5 → 14m	30.3	1.52	54.6	59.6

w: natural soil moisture, e: initial void index, n: porosity, S<sub>r</sub>: saturation degree,

In order to identify the potential for collapse, conventional and simple edometric tests were carried out, without suction control, in accordance with the procedures adopted from ASTM D 2435-04. In order to define the collapsibility of the surface layer, samples were taken at depths between 1.5 m and 6.5 m to be subjected to oedometer tests with and without pre-flooding. The loading stress values adopted were 13 kPa, 25 kPa, 50 kPa, 100 kPa, 200 kPa, 400 kPa, 800 kPa and 1600 kPa. Test specimens were molded from samples collected at depths of 1.5 m, 2.5 m, 4.5 m and 5.5 m.

The criterion adopted to quantify the collapse index (R<sub>w</sub>) was that of Vargas (1978), according to

expression (1). The soil is considered collapsible when its value is greater than 2%.

$$R_w = \left( \frac{e_p - e_w}{1 + e_p} \right) \times 100 \quad (1)$$

where:

- R<sub>w</sub>: subsidence index;
- e<sub>w</sub>: void ratio after flooding the test specimen;
- e<sub>p</sub>: void ratio before flooding the test specimen.

Due to the heterogeneity of the samples, represented by the different initial void ratio values (Table 2).

Table 2: Values of the Void Index

	Sample Depth			
	1.5 m	2.5 m	4.5 m	5.5 m
e <sub>0</sub>	2.14	1.74	1.72	1.66

The results of the tests in saturated and unsaturated conditions are shown in Table 3.

*Table 3:* Pre-Consolidation Stress Values (Natural and Flooded)

Depth (m)	Pre-Consolidation Stress		$\sigma_{av'}^{\text{flooded}} / \sigma_{av'}^{\text{natural}}$
	$\sigma_{av'}$ (kPa) Flooded	$\sigma_{av'}$ (kPa) Natural	
1.5	18	63	0.29
2.5	30	110	0.27
4.5	110	230	0.48
5.5	105	300	0.35

Table 3 shows a reduction in the pre-consolidation stress in the flooded condition, with the reduction varying from 1/3 to 1/2 of the value of the stress in the natural condition. This behavior is related to the influence of the soil's initial moisture conditions, which in turn are closely linked to the suction values. When moistened, these soils lose the resistance between grains or micro-aggregates given by matric suction, as well as having their bonds due to cementation weakened by the increase in

moisture and, jointly, with the application and magnitude of the load.

Figure 2 shows that the samples presented collapsible behavior, with collapse index values greater than 2% at all flood loads (except for sample 4.5 m flooded at load 50 kPa). The  $R_w$  values practically increase with the increase in loading, but tend to stabilize as the depth increases.

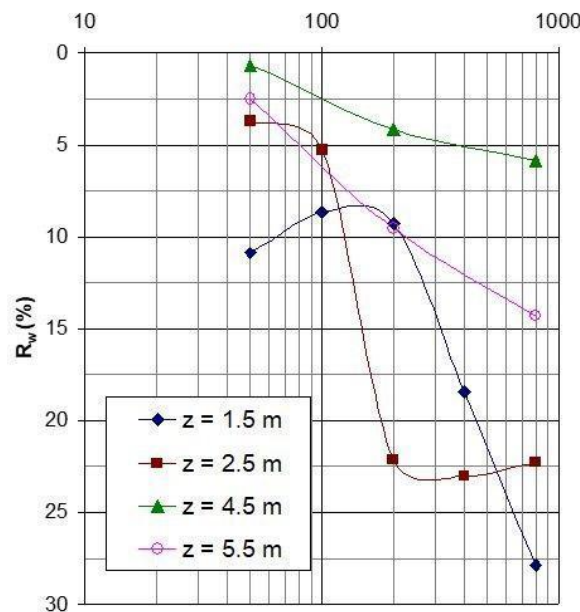


*Figure 2:* Collapse Index vs  $\text{Log}\sigma$

The values in Tables 2 and 3 and the collapse index ( $R_w$ ), as a function of flood stress, shown in Figure 2, the relationship between the values of pre-consolidation stress (virtual or yield) and  $R_w$  is striking. In other words, as the values of this stress increase, the collapse index values decrease and tend to stabilize.

Overall, the information obtained from CPTu and SPT-T tests, regarding soil type and resistance

parameters in unsaturated conditions, allows to state that the soil in the experimental field is of low resistance and high collapsibility.

### III. PILE CONSTRUCTION AND LOAD TESTS

The study used a bored pile with a diameter of 0.40 m and a depth of 12 m, and a continuous flight auger (CFA) pile with the same dimensions.

The longitudinal reinforcement of the piles consisted of  $4\phi_b$  16.0mm ( $\cong 8 \text{ cm}^2$ ), 6 m long and stirrups of  $\phi_b = 6.4\text{mm}$ , every 20 cm (CA-50 steel).

For the bored piles, the concrete  $f_{ck}$  (slump  $\pm 70\text{mm}$ ) was around 15 MPa, using gravel and sand. The concrete used in the continuous auger pile (pumpable, slump  $\pm 240\text{mm}$ ) consumed cement at a rate of  $400 \text{ kg/m}^3$  and aggregates (sand and gravel). The CFA pile was drilled using the MAIT HR-200 drill rig, which can drill diameters of up to 1200 mm and depths of up to

32m. The piles followed a predefined alignment and the spacing between them was 2.4m ( $6\phi$ ).

The following elements were used to carry out the load tests: a 100 kN hydraulic jack, a 100 kN load cell, two deflectometers with a precision of 0.01 mm and a kneecap. All these elements were hollow and to prevent the system from becoming unstable during the tests, a steel bar was passed between them and fitted into two recesses made in the piles (Figures 3 and 4).



Figure 3: View of the Load Test Assembly



Figure 4: Assembly Detail

The load tests were of the quick maintained load (QML), following the requirements of NBR 12.131/1991. The load increments were 3 kN for the load test with natural soil and 2 kN for the pre-flooded situation. Unloading was carried out at predetermined intervals. Two loading and unloading cycles were carried out.

## VI. RESULTS AND ANALYZES

The results obtained from the load tests are presented below, two (first and second) with the soil in its natural condition and the third after pre-flooding the ground for a period of 72 hours. Table 4 shows a summary of the results of the load tests carried out.

*Table 4:* Load and Displacement Maximum Values

Pile	Condition	Load (kN)	Displacement (mm)
Bored	Natural – 1st	54.0	7.82
	Natural – 2nd	67.5	21.20
	Flooded	13.0	13.66
CFA	Natural – 1st	54.5	11.02
	Natural – 2nd	67.5	33.76
	Flooded	13.0	30.26

The figures 5a and 5b show the load vs. displacement curves, with the first and second cycles and with pre-flooding of the ground. Using the methodology proposed by Matlock and Reese (1961), figures 6a and 6b show the horizontal reaction curves of the soil ( $n_h$ ) vs. displacement of the pile on the ground surface ( $y_o$ ), obtained from

the results of the tests carried out with the soil in its natural and flooded condition, assuming that the horizontal reaction modulus of the soil varies linearly with depth. For the case of the piles under analysis,  $n_h$  was defined. for the 6.0 to 12.0mm range (Table 4).

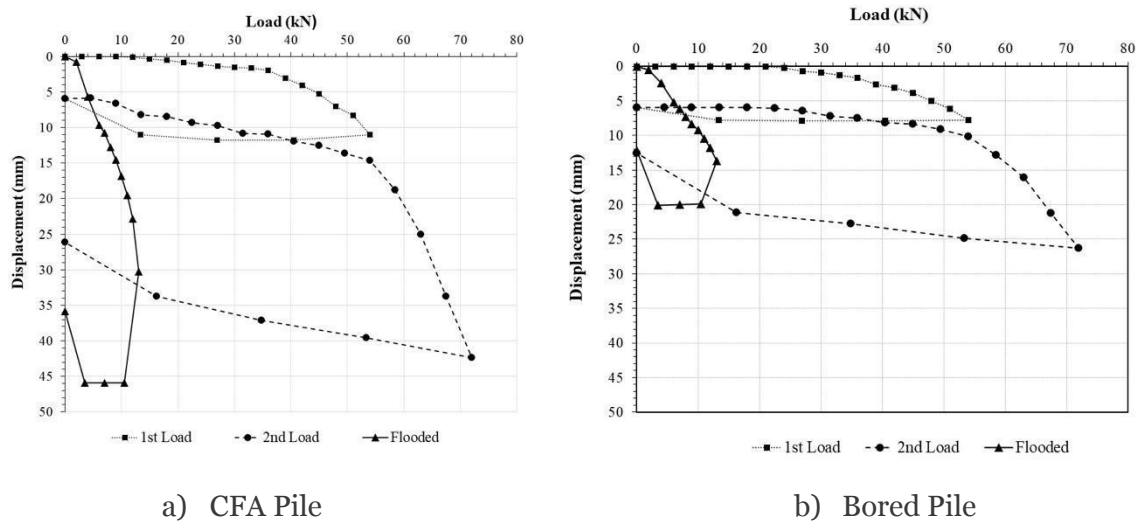


*Figure 5:* Load vs. Displacement Curve

The Figures 5a and 5b show that the pre-flooding of the soil caused a pronounced increase in the displacements for the same load applied in the tests with natural soil. The results proved that the pre-flooding caused a reduction of the applied load by 2.5 to 3.0 times when compared to the natural ultimate load. These results demonstrate the intensity of the effect of the variation of the soil moisture on the horizontal displacement characteristics of the pile.

capacity of the soil of 85% in the third loading, with the soil pre-flooded.

In the third loading, with the soil already flooded, there is a large loss of bearing capacity of the pile, showing the effect of the collapsible characteristic of the soil in this type of loading. For the same value of maximum displacement as the second loading, there is a reduction in the bearing



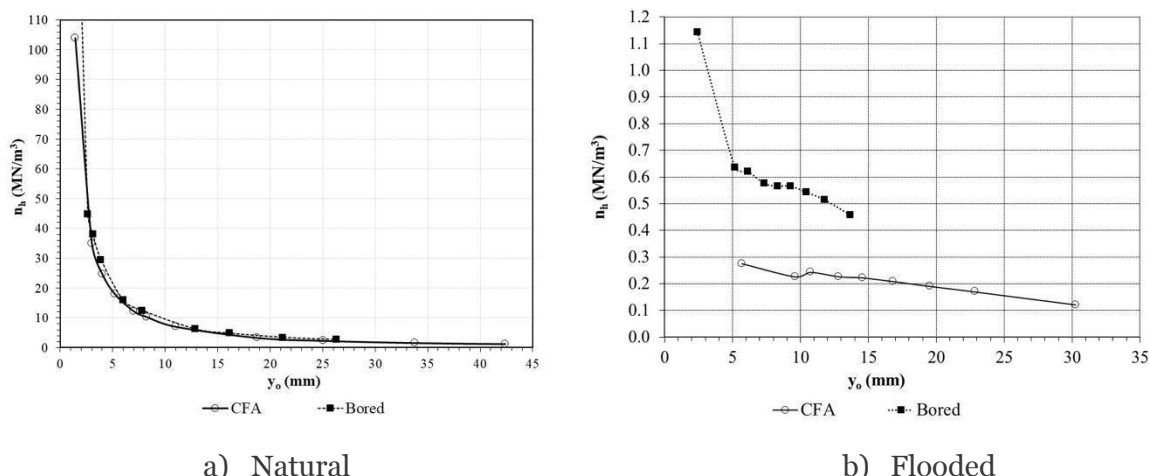


Figure 6:  $n_h$  vs  $y_o$  Curves– Natural and Flooded

It can be seen in Figure 6a that the behavior of the  $n_h$  vs  $y_o$  curves were very similar for the two types of pile, showing that the soil reaction did not vary, even though they were two different types of pile construction processes. The horizontal reaction coefficient (natural moisture) for the bored pile was  $11.8 \text{ MN/m}^3$  and for the CFA pile  $10.3 \text{ MN/m}^3$ . Note that the  $n_h$  values in the pre-flooded

situation practically do not vary, which demonstrates a resistance loss of the soil from the beginning of loading (Figure 6b).

The values of the horizontal soil reaction coefficient  $n_h$ , obtained for displacements of 6 to 12mm, are shown in Table 5.

Table 5:  $n_h$  values

Pile	Condition	$n_h$ (MN/m <sup>3</sup> )	Condition	$n_h$ (MN/m <sup>3</sup> )
Bored	Natural	11.8	Flooded	0.58
CFA	Natural	10.3	Flooded	0.24

The values for the horizontal reaction coefficients obtained in the literature for different types of deep foundations built on soil with similar behavior to the one from the present study (under natural and pre-flooded conditions) (Kassouf, Carvalho and Albuquerque, 2016; Barbosa et al., 2023)

#### IV. CONCLUSIONS

- The oedometer tests showed that the deformations in the samples after being subjected to the tests were characterized, firstly, by the closure of the pores, and then by the sliding of the microaggregates (lumps), in this case, under the tension of 800kPa.
- Since the first meter of soil has a strong influence on horizontal loading, proper geotechnical characterization in terms of porosity, resistance and collapsibility is

important. Laboratory and field tests indicate that soils are highly porous, low resistance collapsible soils, making it possible to predict the large effects of low  $n_h$  values and changes in soil moisture content.

- It has been observed that loads on pre-flooded soils are on average three times lower than soils with natural moisture content until a certain level of displacement is reached. For the soil horizontal reaction coefficient, the pre-flooded values are about 50% lower than those for the natural moisture content of the soil.
- The average horizontal reaction coefficient obtained for soils at natural moisture content is  $11 \text{ MN/m}^3$ , which is higher compared to the literature for high porosity soils, where the recommended value is  $2 \text{ MN/m}^3$ , emphasizing the importance of its determination for each soil type, to avoid generalizations. In the

flooded condition, the soil horizontal reaction coefficient showed an average reduction of approximately 96 % when compared to the natural condition.

- The results indicate that, after loading, there is little recovery of the displacement occurred by the pile during unloading. In a second loading, until the maximum load of the first loading is reached, the pile suffers little displacement. From this maximum load onwards, in the second loading, the curve takes on the continuity of the curve from the first loading, as can be seen in figure 5.

### ACKNOWLEDGMENTS

The authors gratefully acknowledge to the support of the Universidade Estadual de Campinas (UNICAMP).

### REFERENCES

1. ABNT NBR 12.131 (1991) Static load test (*in portuguese*).
2. Albuquerque, P.J.R.; Carvalho, D.; Kassouf, R., Fonte Jr., N.L. (2019) Behavior of Laterally Top-Loaded Deep Foundations in Highly Porous and Collapsible Soil. *Journal of Materials in Civil Engineering*. V.31 -2. [https://doi.org/10.1061/\(ASCE\)MT.1943-5533.00025](https://doi.org/10.1061/(ASCE)MT.1943-5533.00025).
3. Albuquerque, P.J.R.; Massad, F., Viana da Fonseca, A.; Carvalho, D.; Santos, J.; Esteves, E.C. (2011) Effects of the construction method on pile performance: evaluation by instrumentation. part 1: experimental site at the State University of Campinas. V.34(1): 35-50, January-April. <https://doi.org/10.28927/SR.341035>.
4. ASTM D 2435 (2004) Standard test methods for one-dimensional consolidation properties of soils using incremental loading.
5. Barbosa, Y., Tarozzo, M.H.P.; Albuquerque, P.J.R. and Carvalho, D., (2023) Behavior of a new laterally top-loaded post-grouted micropile in highly porous lateritic soil. *DYNA*, 90 (225), pp. 123-131, January – March. <https://doi.org/10.15446/dyna.v90n225.104807>.
6. Broms, B.B. (1964) Lateral resistance of piles in cohesionless Soils. *Journal of Soil Mechanics and Foundation Engineering Division, ASCE* 90, SM-3, p.123-1564.
7. Carvalho, D.; Albuquerque, P.J.R.; Claro, A.T.; Ferreira, C.V. (1996) Analysis of a pile loaded transversely at the top in residual diabase soil. *Proceedings of 3º Seminário de Engenharia de Fundações Especiais - S.E.F.E. III, São Paulo, 1996, Anais, Vol. 1, 145-154. (in portuguese)*
8. Carvalho, D.; Albuquerque, P.J.R.; Giacheti, H.L. (2000) Experimental field for soil mechanics and foundations studies in Campinas. *Proceedings of 4º Seminário de Engenharia de Fundações Especiais - S.E.F.E. IV, São Paulo, 2000, Anais, Vol.3, 79-87. (in portuguese)*
9. Davisson, M. T. (1970) Lateral load capacity of piles. *Highway Research Record*, n. 333, Pile Foundations, National Research Council, Washington, D.C., p.104-112.
10. Davisson, M.T.; Gill, H.L. (1963) Laterally loaded piles in a layered soil system. *Journal of the Soil Mechanics and Foundation Division, ASCE*, vol. 89, SM-3, p.63-94.
11. Dudley, J.H. (1970) Review of Collapsing Soils. *Journal of the Soil Mechanics and Foundation Division. ASCE*, Vol. 96, n. SM3, 925-947.
12. García, F.J.A., Cunha, R.P., Albuquerque, P.J.R.; Farias, M.M.; Bernardes, H.C. (2023) Experimental and Numerical Behavior of Horizontally Loaded Piled Rafts with a Defective Pile. *Geotech Geol Eng* 41, 429–439. <https://doi.org/10.1007/s10706-022-02288-2>
13. Jennings, J.E.; Knight, K. (1957) The Additional Settlement of Foundations Due to a Collapse of Structure of Sandy Sub Soils on Wetting. *Proceedings of IV International Conference on Soil Mechanics And Foundation Engineering. Proceedings. Vol.1, London, 316-319.*
14. Kassouf, R., Carvalho, D.; Albuquerque, P. J. R. (2016) The behavior of a foundation transversally loaded at the top over highly porous and collapsible soil *DYNA* 83 (199) pp. 134-139, <https://doi.org/10.15446/dyna.v83n199.52529>.

15. Matlock, H.; Reese, L.C. (1960). Generalized solutions for laterally loaded piles. *Journal of Soil Mechanics and Foundation Engineering Division - ASCE*, 86 (SM5), p. 63-91.
16. Matlock, H.; Reese, L.C. (1961) Foundation analysis of offshore pile supported structures. *Proceedings of International Conference on Soil Mechanics and Geotechnical Engineering*, 5, v. 2, p. 91-97.
17. Matlock, H.; Reese, L.C. (1961) Generalized solutions for laterally loaded piles. *Journal of the Soil Mechanics and Foundation division, ASCE*, Vol.86, SM5, 63-91.
18. Miche, R.J. (1930) Investigation of piles subjected to horizontal force. Application to quay walls. *Journal of the School of Engineering*, n. 4, Giza, Egypt.
19. Palmer, L.A.; Thompson, J.B. (1948) The Earth pressure and deflection along the embedded lengths of piles subject to lateral thrusts". *Proceedings of 2<sup>nd</sup> International Conferences on Soil Mechanics and Foundation Engineering*. Rotterdam, vol.5, p.156-161.
20. Poulos, H.G. (1971) Behavior of laterally loaded piles: I – Single Piles. *Journal of the Soil Mechanics and Foundation Engineering Division, ASCE* 9795, p.711-731.
21. Poulos, H.G.; David, E.H. (1980) *Pile Foundation analysis and Design*. John Wiley and Sons, New York, USA, 357p.
22. Rosendo, D.C.; Albuquerque, P.J.R. (2021) General analytical solution for laterally loaded pile based Miche model. *Geotech Geol Eng* 39, 765–782.  
<https://doi.org/10.1007/s10706-020-01520-1>
23. Terzaghi, K. (1955) Evaluation of coefficients of subgrade reaction. *Géotechnique*, 5 (4), p. 297-326.
24. Vargas, M (1978) *Introduction to soil mechanics*. McGraw-Hill do Brasil, Editora da Universidade de São Paulo, São Paulo, 509p. (*in portuguese*)

*This page is intentionally left blank*



Scan to know paper details and  
author's profile

# Comparison of Thermal Numerical Simulation Data with Experimental Data from the ISCT 200-US Permanent Magnet Hall Thruster

*Marconi C. Porto, Alexandre A. Martins, José Leonardo Ferreira & Carlos Humberto Llanos*

*University of Brasilia*

## ABSTRACT

Due to its great efficiency, the Plasma Physics Laboratory of the Physics Institute of the University of Brasilia (PPL/PI/UnB) has been developing Hall thrusters since 2004. Testing NeFe and SmCo permanent magnets, excellent results were achieved with the PHALL II series (PPL). However, permanent magnets have limitations due to the working temperature (determined by the Curie temperature). Therefore, it is necessary to strictly control its temperature to avoid the demagnetization effect.

In this work, the results of the numerical thermal simulation were compared with experimental temperature results for the ISCT200-US Hall Thruster in order to verify the reliability of the simulation tool, allowing its future use in simulations of other Hall thrusters. Experimental temperature values and, whenever possible, dimensions and materials of the propellant components were collected from references on the ISCT200-US. A mechanical drawing of the ISCT 200-US was created, a numerical thermal simulation was developed, temperature simulation values were collected and compared with experimental values.

**Keywords:** hall thruster electric propulsion thermal numerical simulation ISCT 200-US thermal dissipation aerospace.

**Classification:** LCC Code: TL787-TL4050

**Language:** English



Great Britain  
Journals Press

LJP Copyright ID: 392922

Print ISSN: 2631-8474

Online ISSN: 2631-8482

London Journal of Engineering Research

Volume 23 | Issue 5 | Compilation 1.0



© 2023. Marconi C. Porto, Alexandre A. Martins, José Leonardo Ferreira & Carlos Humberto Llanos. This is a research/review paper, distributed under the terms of the Creative Commons Attribution-Noncommercial 4.0 Unported License <http://creativecommons.org/licenses/by-nc/4.0/>, permitting all noncommercial use, distribution, and reproduction in any medium, provided the original work is properly cited.



# Comparison of Thermal Numerical Simulation Data with Experimental Data from the ISCT 200-US Permanent Magnet Hall Thruster

Marconi C. Porto<sup>α</sup>, Alexandre A. Martins<sup>σ</sup>, José Leonardo Ferreira<sup>ρ</sup>  
& Carlos Humberto Llanos<sup>ω</sup>

## ABSTRACT

*Due to its great efficiency, the Plasma Physics Laboratory of the Physics Institute of the University of Brasilia (PPL/PI/UnB) has been developing Hall thrusters since 2004. Testing NeFe and SmCo permanent magnets, excellent results were achieved with the PHALL II series (PPL). However, permanent magnets have limitations due to the working temperature (determined by the Curie temperature). Therefore, it is necessary to strictly control its temperature to avoid the demagnetization effect.*

*In this work, the results of the numerical thermal simulation were compared with experimental temperature results for the ISCT200-US Hall Thruster in order to verify the reliability of the simulation tool, allowing its future use in simulations of other Hall thrusters. Experimental temperature values and, whenever possible, dimensions and materials of the propellant components were collected from references on the ISCT200-US. A mechanical drawing of the ISCT 200-US was created, a numerical thermal simulation was developed, temperature simulation values were collected and compared with experimental values. A coherent comparison was achieved, which demonstrated the reliability of the simulation tool. Such results are important for the space qualification of thrusters subsequent to the PHALL II series.*

**Keywords:** hall thruster electric propulsion thermal numerical simulation ISCT 200-US thermal dissipation aerospace.

**Author α σ ρ:** Plasma Physics Laboratory, Physics Institute, University of Brasilia, Brasilia, Brazil.

**α ω:** Embedded Systems and Integrated Circuit Applications Laboratory, Mechanical Engineering Department, University of Brasilia, Brasilia, Brazil.

## I. INTRODUCTION

Hall thrusters are considered a type of electric thruster [1-6]. The main characteristic of an electric thruster is the ability to produce plasma by ionization of a neutral gas, by the inclusion of electric and magnetic fields in its medium, and generate impulse for its acceleration of the thruster. Normally used to correct the orbit and attitude of artificial satellites and the propulsion of space probes, the Hall thruster has as its basic shape a cylindrical channel, an anode at the bottom of this channel, a magnetic field inside the channel and an external cathode [6]. Its operation consists of injecting a neutral gas into the channel, emitting electrons from the cathode towards the anode; the thruster then confines the electrons in an ExB Hall current that creates a virtual cathode above the anode. In this way, the electric field between the anode and the virtual cathode accelerates the ions out of the channel, generating thrust. The first flight tests of the Hall thruster took place in the 1960s [1,5-7].

The Physics Laboratory of the Physics Institute of the University of Brasilia (PPL/PI/UnB) has been developing Hall Thrusters since 2004 [1,2,8,9] under the name PHALL Project. It is an incremental project, having started with PHALL I, followed by PHALL II-A, PHALL II-B and currently the PHALL II-C version (Fig. 1 and 2). The current version has a TRL 3 classification (Technology Readiness Level, NASA). The next, more compact and efficient version, to be developed by PPL, supported by the Brazilian

Space Agency (AEB), is the PHALL III [1] to reach TRL 6. The ultimate objective is to develop a Hall thruster for micro and small artificial satellites fully qualified for spaceflight with TRL 9

classification. Other PPL work includes an HPT thruster (Fig. 3) in different versions, elimination of biological contaminants using plasmas and deposition of thin carbon films.

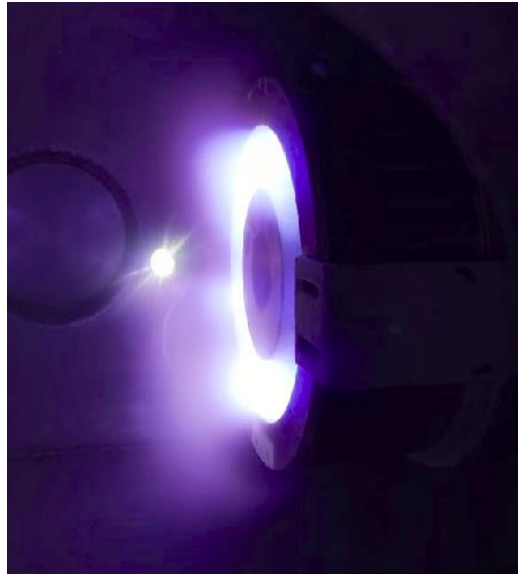


*Fig. 1:* Side View of PHALL II-C in Operation (PPL/PI/UnB)

The present work aims to verify the reliability of a thermal numerical simulation strategy and corroborate the results obtained in a similar work

carried out by PPL with the BPT-4000 thruster [11]. Such confirmation will allow future tests with PHALL III and its subsequent versions.

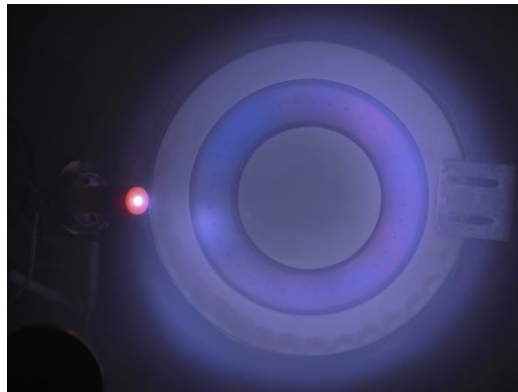


*Fig. 2:* Front view of PHALL II-C in operation (PPL/PI/UnB)

A systematic bibliographic research was carried out to find articles in which Hall thruster experiments with sufficient data to perform a simulation were presented. No studies were found that compared results from experiments and thermal simulations. Thus, the main advantage of the results of this study in relation to other experimental and thermal simulation studies is the fact that they indicate good reliability for commercial simulation software widely used in relation to thermal simulations of

Hall Thrusters. In this research, few options were found, two of which were advantageous for developing work like this: one option was the Hall BPT4000 thruster (discharge power of 4500 W, electromagnetic coils), the study of which was developed by PPL in [11]; and the other option was the Hall ISCT200-US thruster (200 W discharge power, permanent magnets), the study of which is developed in the present work. The study carried out proposes to carry out a study that presents a good approximation between the



contexts of the PHALL II-C and ISCT200-US thrusters and not necessarily something extremely precise or exact to give direction to

future work that approach thermal numerical simulations through the technique of finite elements.

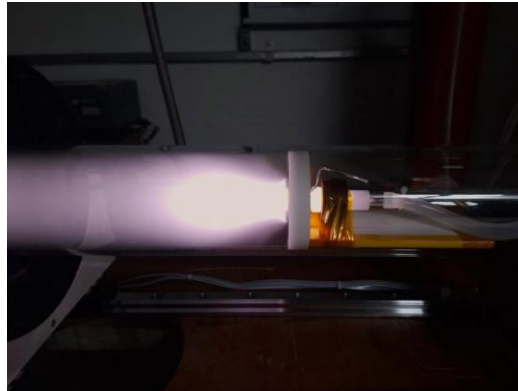


*Fig. 3: HPT Thruster in Operation (PPL/PI/UnB)*

The experimental data of the ISCT 200-US thruster [10] was collected from the literature and then thermal numerical simulation of this thruster was carried out. The simulation temperatures obtained were compared with the experimental ones, observing a good agreement with experimental data, with a small percentage difference. This fact indicates that this approach, based on finite elements, has good reliability on the Hall thruster simulation task, in addition to corroborating the results found in [11] for the BPT-4000 thruster.

Two software were considered to be used in the simulations, SolidWorks 2017 and Ansys 2017. Although a detailed benchmark was not performed, the Solid Works 2017 software proved to be the best option because the thermal model used by this software was found, but was not found for Ansys 2017 software. Additionally, SolidWorks 2017 has simpler CAD handling and is probably better known.

In future PPL work, supported by AEB, we will carry out an experiment to thermal study the PHALL III (next version) and, later, we will carry out a more precise comparison study with simulation software.

The main contributions of the present work are the following: (a) a verification of the reliability of a thermal numerical simulation of Hall thrusters (such a comparison between simulation and experiment was not found in the literature), (b) a

verification of the equations for dissipated thermal powers in Hall thrusters (definition of an appropriate configuration of equations to support the system modeling problem using the finite element technique), (c) Corroboration of the results of this work with the results obtained in [11], with the exception that, this time, the thruster's magnetic field is generated by permanent magnets.

As a description of the sections of the article, we have: (a) section 2, which describes the methodology, (b) section 3, which presents the mathematical models, (c) section 4, with the results and their analysis, and (d) section 5, presenting the most relevant conclusions.

## II. METHODOLOGY

Below is, in summary form (with greater detail in the subsections), the procedure adopted.

- 1) From reference [10], the experimental temperatures of the ISCT 200-US thruster were collected.
- 2) The thermal power dissipated generated by the thruster was calculated.
- 3) The materials for the ISCT 200-US components were selected.
- 4) The 3D CAD mechanical drawing was copied from the references.
- 5) Simulated and experimental temperature data were compared.

### 2.1 Experimental Temperatures

From Ref. [10], the average experimental temperatures were consulted in the following

parts of the thruster: anode, internal wall and external wall (blue in Fig. 4).

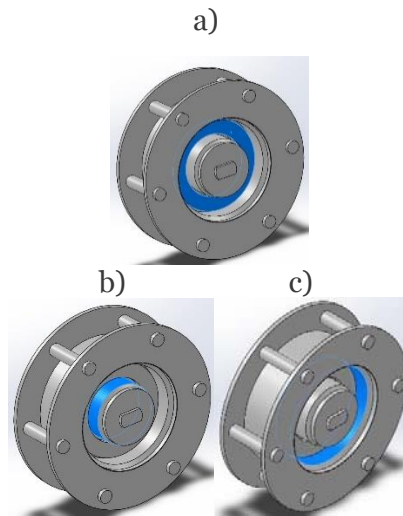


**Fig. 4:** Regions (in blue) of the ISCT200-US Where Experimental Temperatures Were Measured: (A) Anode, (b) Inner Wall, and (c) Outer Wall

Such temperatures are given in Table 1. No data were found in the literature on thermal contact resistances related to ISCT 200-US. Another way to obtain this data would be through temperature

measurement in experiments on a real physical model, which was not viable. Therefore, thermal contact resistances were disregarded in the simulation.

**Table 1:** Average Experimental Temperatures of the ISCT 200US

ISCT200-US	Anode (°C)	Inner Wall (°C)	Outer Wall (°C)
Experiment	440.00	420.00	413.00

### 2.2 Dissipated Thermal Powers

The following steps were followed in order to determine the dissipated thermal powers used in the ISCT 200-US simulation: some internal experimental data from PHALL II-C (such as, for example, plasma potential, floating potential and electron density) were used in the model for thermal energy dissipation [6,12] to calculate the power dissipated in PHALL II-C. After that, using the power dissipated in the PHALL IIC, the power dissipated in the ISCT 200-US was calculated proportionally to the discharge power of the PHALL II-C (subsection 3.1).

### 2.3 ISCT 200-US materials and mechanical drawing

With the help of information found in works [10,14,15,17], the mechanical drawing in 3D CAD

was generated. Fig. 5 shows the exploded view of the mechanical drawing. Because they have little influence on heating and to speed up the simulation process, the fasteners were omitted. Fig. 6 shows a perspective view of the assembled thruster. In Table 2, you can find the main measurements of the mechanical drawing of the ISCT200-US compared to the measurements of the PHALL II-C. And in Fig. 7, there is a perspective view of PHALL II-C.

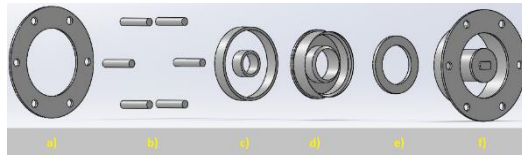


*Fig. 5:* Exploded View of the Mechanical Drawing of the ISCT200-US Thruster. From Left to Right: (a) Base Piece, (b) 6 Tubes for Heat Transmission, (c) Representation of Permanent Magnets, (d) Ceramics, (e) Anode, and (f) Structure

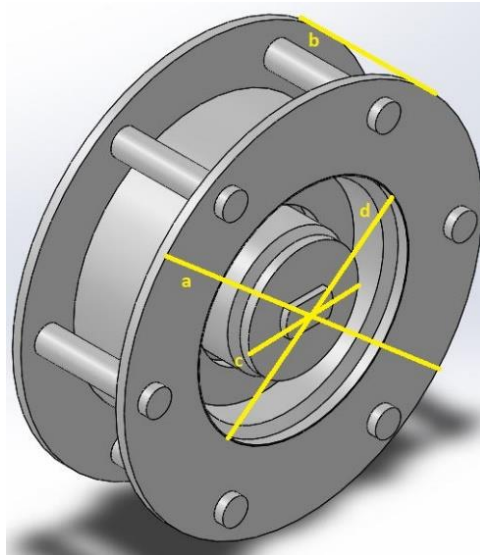


*Fig. 6:* Perspective View of the Mechanical Drawing of the ISCT200-US Thruster

The materials were consulted in works [10,14-17] related to the ISCT 200-US thruster, as far as possible. When there was not enough information, the same materials (or similar

materials) as the PHALL II-C thruster were used. The materials used in the simulation are presented with the relevant physical properties in Table 3.

*Table 2:* Main measurements of the Mechanical Drawing for the Simulation of the ISCT200-US (Figure 6) and the PHALL II-C (Figure 7)

Part of the Thruster	Values (mm)	
	ISCT200-US	PHALL II-C
Front View Diameter	85.00 (a)	151.40 (e)
Length	26.50 (b)	82.28 (f)
Discharge Channel Internal Diameter	26.00 (c)	68.01 (g)
Discharge Channel External Diameter	49.50 (d)	114.14 (h)

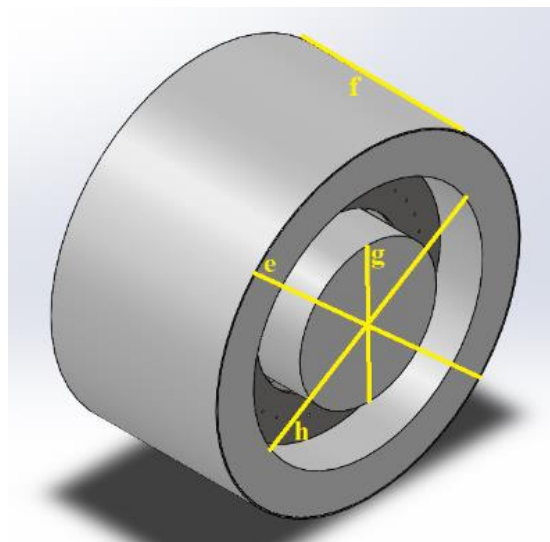


Fig. 7: Perspective View of the Mechanical Drawing of the PHALL II-C Thruster

Table 3: Materials of the ISCT200-US Components and Their Physical Properties

Component	Material	Mass Density (kg/m <sup>3</sup> )	Thermal Conductivity (W/mK)	Specific Heat (J/kgK)	Emissivity
Structure	Stainless Steel 301	7880.00	21.40	500.00	0.59
Base Piece	Stainless Steel 301	7880.00	21.40	500.00	0.59
Anode	Stainless Steel 304 [16,17]	8000.00	16.20	500.00	0.19
Ceramics	BN-SiO <sub>2</sub> [10,14-17]	2100.00	11.00	770.00	0.90
Tubes	Copper [16,17]	8900.00	390.00	390.00	0.75
Permanent magnets	Sm <sub>2</sub> Co <sub>17</sub> [16,17]	8400.00	11.63	376.81	0.11

### III. MATHEMATICAL MODELS

#### 3.1 Model for Thermal Energy Dissipation

The dissipated thermal power values used for the ISCT200-US thruster simulation were calculated proportionally to the same values for the PHALL II-C thruster. To calculate the dissipated thermal powers of the PHALL II-C, a model for thermal energy dissipation in Hall thrusters [6,12] was used, into which the thruster thruster plasma data can be inserted. The equation for the discharge power  $P_d$  [12] is:

$$P_d = P_b + P_w + P_a + P_r + P_{ions}, \quad (1)$$

where  $P_b$  is the beam power,  $P_w$  is the power dissipated in the walls,  $P_a$  is the power dissipated in the anode,  $P_r$  is the radiative power loss from the plasma, and  $P_{ions}$  is the power to produce ions.

The beam power is defined by the equation:

$$P_b = V_b I_b, \quad (2)$$

where  $V_b$  is the beam voltage,  $I_b$  is the beam current. The following equation is the power dissipated in the walls:

$$P_w = n_e e A_w \left[ \left( \frac{kT_e}{e} \right)^{\frac{3}{2}} \left( \frac{2e}{\pi m} \right)^{\frac{1}{2}} e^{\frac{e\phi_s}{kT_e}} + \frac{1}{2} \left( \frac{kT_e}{M} \right)^{\frac{1}{2}} (\epsilon - \phi_s) \right], \quad (3)$$

where  $n_e$  is the electronic density,  $e$  is the electron charge with positive value,  $A_w$  is the surface area of the wall in contact with the plasma,  $k$  is the Boltzmann constant,  $T_e$  is the temperature electronic in Kelvins,  $m$  is the electron mass,  $\phi_s$  is the sheath potential relative to the plasma ( $-V_f$ ),  $M$  is the mas of the Argon atom (PHALL II-C propellant), and  $\varepsilon$  is the pre-sheath ion energy. The power dissipated in the anode can be calculated by the following equation:

$$P_a = 2T_{ev}I_a \approx 2T_{ev}I_d, \quad (4)$$

where  $T_{ev}$  is the electronic temperature in electron-volts,  $I_a$  is the anode current, and  $I_d$  is the discharge current. The following equation represents the radiative power loss from the plasma:

$$P_r = n_o n_e \langle \sigma * v_e \rangle V_{pr}, \quad (5)$$

where  $n_o$  is the neutral density,  $\langle \sigma * v_e \rangle$  is the excitation rate coefficient that includes the excitation cross-section and the electron velocity, and  $V_{pr}$  is the volume of the high temperature plasma region. For the power to produce ions, we have the following equation:

$$P_{ions} = (I_b + I_{iw})U^+, \quad (6)$$

where  $I_{iw}$  is the ionic current to the wall, and  $U^+$  ionization potential. The following equation was used for the pre-sheath ion energy [6]:

$$\varepsilon = 0.58 \frac{kT_e}{e}. \quad (7)$$

The equations effectively used to calculate the dissipated thermal powers in the walls and in the anode (parts in contact with the plasma) were equations (3), (4) and (7). First, the total dissipated thermal power in the walls and the dissipated thermal power in the anode were calculated for the PHALL II-C, both for the discharge power of 195.00W and for 470.53W. The values of the parameters used in the equations can be found in Table 4 (in the case of the values measured experimentally) and in Table 5, while the values of the calculated powers can be found in Table 6. The values obtained experimentally are internal experimental data and were measured using a Langmuir probe, whose tip was placed in the plasma plume 20cm from the PHALL II-C thruster.

From Table 4,  $V_p$  is the plasma potential,  $V_f$  is the floating potential,  $T_{ev}$  is the electron temperature in electron-volts, and  $n_e$  is the electron density.

Table 4: Average Data for PHALL II-C Performance

Parameters	Discharge Power 195.00W (Anode: 78.00V, 2.50A)	Discharge Power 470.53W (Anode: 105.50V, 4.46A)
$V_p$ (V)	77.00	104.00
$V_f$ (V)	8.00	10.00
$T_{ev}$ (eV)	4.28	5.61
$n_e$ ( $m^{-3}$ )	$2.06 \times 10^{16}$	$2.13 \times 10^{16}$

Table 5: Data for PHALL II-C

Parameters	Discharge Power 195.00W (Anode: 78.00V, 2.50A)	Discharge Power 470.53W (Anode: 105.50V, 4.46A)
$T_e$ (K)	49667.26	65101.25
$I_d$ (A)	2.50	4.46
$e$ (C)	$1.60 \times 10^{19}$	$1.60 \times 10^{19}$
$A_w$ ( $m^2$ )	$3.76 \times 10^{-3}$	$3.76 \times 10^{-3}$
$k$ (J/K)	$1.38 \times 10^{-23}$	$1.38 \times 10^{-23}$
$m$ (kg)	$9.11 \times 10^{-31}$	$9.11 \times 10^{-31}$
$M$ (kg)	$6.63 \times 10^{-26}$	$6.63 \times 10^{-26}$
$\phi_s$ (V)	-8.00	-10.00
$\varepsilon$ (V)	2.48	3.25

Then, the ratios for walls, equation (8), and anode, equation (9), between the values of dissipated thermal power and discharge power

were calculated for both the 195.00W case and the 470.53W case. After that, the average between

the two cases was calculated (Table 7). The ratio equations are shown below:

$$R_w = \frac{P_w}{P_d}, \tag{8}$$

$$R_a = \frac{P_a}{P_d}. \tag{9}$$

Where  $R_w$  is the ratio for walls,  $P_w$  is the power dissipated in the walls,  $P_d$  is the discharge power,

$R_a$  is the ratio for anode and  $P_a$  is the power dissipated in the anode.

These ratios calculated for the walls and for the anode were used to calculate, proportionally to the discharge power of the ISCT200-US, the total dissipated thermal power in the walls and the dissipated thermal power in the anode (Table 8). After that, the dissipated thermal powers in each particular wall were calculated.

*Table 6:* Dissipated Thermal Powers of walls and anode for PHALL II-C

Part of the PHALL II-C	For Disch. Power	For Disch. Power
Walls	58.89W	99.24W
Anode	21.40W	50.04W

We have that in [18] the depositions of thermal energy in the anode in the radial direction and in the internal and external walls of the discharge channel in the axial direction are practically constant, as we put in the simulation of the ISCT200-US; already the reference [19] indicates an almost constant temperature distribution in

the anode and with a small variation in the internal walls (approximately from 910K to 1090K) and external (approximately from 910K to 1080K) of the discharge channel, which corroborates with the distribution of thermal energy deposition in [18]

*Table 7:* Ratios Between the Values of Dissipated Thermal Power and Discharge Power for PHALL II-C

Part of the PHALL II-C	For Disch. Power	For Disch. Power	Average
Walls	0.3020	0.2109	0.2565
Anode	0.1097	0.1064	0.1081

We need the value on each wall for the simulations. The total thermal power dissipated in the walls is the sum of the powers in each wall – see equation (8). The power division used by us was determined by analyzing [13], where the inner wall of the discharge channel heats up more than the outer wall. According to [13], the temperature of the inner wall is higher than the

temperature (550K-600K) of the outer wall of the T-140 HET (Hall thruster) for a discharge power of 630W (the smallest in the study carried out in [13] and the closest to the discharge power of the ISCT200-US). Furthermore, where we have to include analysis of the relationship between the surface areas of the inner and outer walls.

*Table 8:* Dissipated Thermal Powers of Walls and Anode for ISCT200-US

Part of the PHALL II-C	Dissip. Thermal Power (W)
Walls	51.29
Anode	21.61

Such a relationship shows that the area of the inner wall of the PHALL II-C is approximately 60% of the area of its outer wall (the division of

the area of the inner wall by the area of the outer wall is equal to 0.5958). This is an indication that the dissipated thermal power per unit area

(power density) is almost twice as high in the inner wall. Considering also that the magnetic field is stronger at the inner wall, it is expected that it will be subject to more plasma impact along magnetic field lines than the outer wall.

Because of this, a power density (power/area) ratio between the inner and outer walls of about 2:1 is expected, which is the value required to obtain a temperature difference between the inner and outer walls similar to that shown in [13].

For the center and edge walls, located in front of the thruster (Figure 3), the proportion of power density was considered equal to that of the inner wall, due to the deposition shown in PHALL II-C thruster, where the experimental data of plasma

was collected. Equations (10) to (12) below were used to calculate the powers in each wall:

$$P_{wB} = P_o + P_i + P_c + P_e \tag{10}$$

$$n \frac{P_o}{A_o} = \frac{P_i}{A_i} = \frac{P_c}{A_c} = \frac{P_e}{A_e} \tag{11}$$

$$n = 2 \tag{12}$$

where  $P$  is the power in a given wall,  $A$  is the area of a given wall, the subscripts  $o, i, c, e$  refer, respectively, to the outer wall, inner wall, center wall and edge wall, with  $n$  being a factor of proportionality. The blue regions in Figure 6 indicate where the  $P_o, P_i, P_c$  e  $P_e$  powers are applied to the respective surfaces.

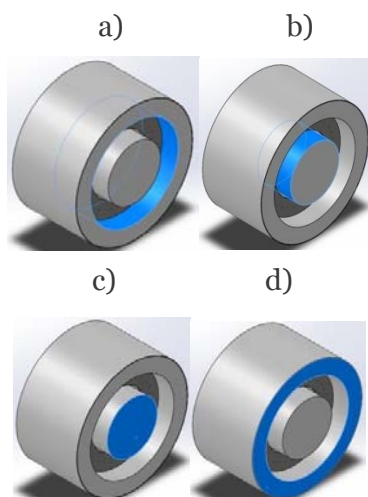


*Fig. 8:* Identification (blue color) of the wall surfaces considered for local power deposition in the PHALL II-C thruster: (a) outer wall,  $P_o$ , (b), inner wall,  $P_i$ , (c) central wall,  $P_c$  and (d) edge wall,  $P_e$

For a discharge power of 200 W, the dissipated thermal powers for each part of the ISCT200-US are found in Table 9.

*Table 9:* Dissipated thermal powers for the ISCT200-US thruster

Part of the ISCT200-US	Power (W)
Anode	21.61
Inner Wall	9.25
Outer Wall	8.17
Central Wall	4.49
Edge Wall	29.38

### 3.2 The Thermal Model

The thermal model was determined from the theoretical manual [20] of the commercial

software used (SolidWorks 2017, from the manufacturer Dassault Systemes). For simulation calculations, the geometry of the solid that forms

the thruster is divided into smaller parts - called finite elements (Figure 9); In this way, the structure of the solid becomes a discrete system

with a set of discrete equations for the thermal model:

$$[C_T] \left[ \frac{\partial T}{\partial t} \right] + [K]\{T\} = \{R\}. \quad (13)$$



Fig. 9: Mechanical Drawing of the ISCT200-US Thruster With the Subdivision of the Solid Into Finite Elements

In this case,  $T$  is the temperature at the element and is given by:

$$T = [D]\{T_n\}, \quad (14)$$

where  $[D]$  is a vector of shape or interpolation functions (depends on the position of the element),  $\{T_n\}$  Is a column vector of nodal temperatures and possible temperature derivatives.  $[C_T]$  is calculated by equation (15).

$$[C_T] = \iiint_{\Delta V} \rho c [D]^T [D] dV, \quad (15)$$

where  $\Delta V$  is the volume of the element,  $\rho$  is the mass density, and  $c$  is the specific heat. The other parameters are calculated according to equations (16) to (18)

$$[K] = [K_T], \quad (16)$$

with

$$[K_T] = \iiint_{\Delta V} [B]^T [k][B] dV, \quad (17)$$

$$[B] = \left\{ \begin{array}{c} \frac{\partial D}{\partial x} \\ \frac{\partial D}{\partial y} \\ \frac{\partial D}{\partial z} \end{array} \right\}. \quad (18)$$

Futhermore,

$$\{R\} = \{R_Q\} - \{R_q\}, \quad (19)$$

where  $[k]$  is the thermal conductivity and being

$$\{R_Q\} = \iiint_{\Delta V} Q [D]^T dV, \quad (20)$$

where  $Q$  is the internally generated heat flux, and the last parameter,  $\{R_q\}$  is calculated as shown in equation (21).

$$\{R_q\} = \iint_{\Delta S_q} q [D]^T dS, \quad (21)$$

where  $\Delta S_q$  is the boundary portion of the element and  $q$  is the boundary heat flux.

## VI. RESULTS AND DISCUSSION

Starting with a simulation diagram of the ISCT200-US (Figure 10), the results obtained in the present work are presented below.



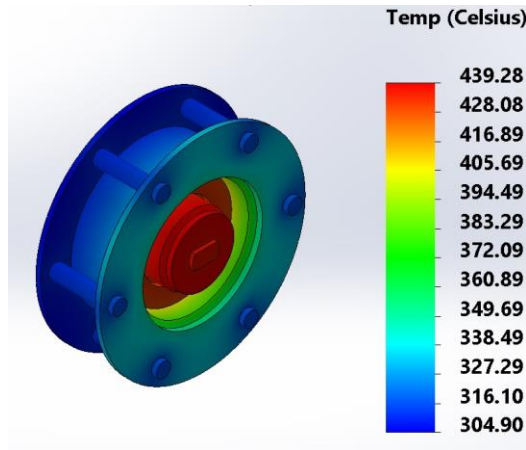


Fig. 10: ISCT200-US thruster simulation diagram

Regarding the three ISCT200-US regions considered in the experiment, the average temperatures achieved in the simulation and the experimental average temperatures presented in reference [10] are available in Table 10.

Table 10: Average Simulation Temperatures and Average Experimental Temperatures for the ISCT200-US Thruster

ISCT200-US	Anode (°C)	Inner Wall (°C)	Outer Wall (°C)
Experiment	440.00	420.00	413.00
Simulation	429.38	436.29	396.32
Difference	10.62	16.29	16.68
Percentage Difference	2.41%	3.88%	4.04%

The results obtained in the three regions considered (anode, internal wall and external wall) were very faithful to those presented by the experiments in reference [10], as a temperature difference (Table 10) between the experimental and simulated values was quite low, with an error (in percentage) having a variation between 2.41% and 4.04%.

It is estimated that the temperature difference between experimental and simulated data would be even smaller if the thermal contact resistances and all materials properly used in the ISCT200-US thruster were included in the simulation.

It is believed that the theoretical reliability of the equations for dissipated thermal power is reinforced due to the fact that they are used in the simulation to confirm the experimental data.

Due to the good results found, with the help of the equations, it appears that the simulation software is reliable.

Therefore, as the results indicate, future simulations of Hall thruster models with permanent magnets carried out using a tool based on finite elements will also be reliable for validation before obtaining experimental data.

These results also corroborate the developments in reference [11], in addition to providing greater precision. In reference [11], similar work was carried out with the BPT-4000 literature thruster.

## V. CONCLUSIONS

A thermal numerical simulation of a Hall thruster found in the literature, called ISCT200-US, was carried out, in which the experimental data

provided by the literature were compared with simulation results in order to verify the reliability of the simulation tool and the corroboration of the results with a work carried out with Hall BPT-4000 thruster. The difference between the experiment and simulation temperatures was small. The percentage of difference varied between 2.41% and 4.04%, which indicates that the simulation software and the approximations used present good reliability when applied to Hall thrusters, in addition to confirming the results found in [11] for the BPT-4000.

### ACKNOWLEDGMENTS

Marconi C. Porto thanks CAPES for the support in the form of a Master's Degree Scholarship.

### REFERENCES

1. J. L. Ferreira, A. A. Martins, R. A. Miranda, M. C. F. Porto, H. O. Coelho, Hall plasma thruster development for micro and nano satellites, *J. Phys.: Conf. Ser.* 1365 012026 (2019).
2. J. L. Ferreira, A. A. Martins, R. A. Miranda, A. Schelling, L. S. Alves, E. G. Costa, H. O. Coelho, A. C. Branco, F. N. O. Lopes, Permanent magnet Hall thruster development and applications on future brazilian space missions, *J. Phys.: Conf. Ser.* 641 012016 (2015).
3. S. Reilly, M. Sekerak, R. Hofer, Transient Thermal Analysis of the 12.5 kW Hermes Hall Thruster, 52<sup>nd</sup> AIAA/SAE/ASEE Joint Prop. Conf. AIAA 2016-5024 (2016).
4. N. Turan, U. Kokal, M. Celik, H. Kurt, Experimental Study of the Effects of the Cathode Position and the Electrical Circuit Configuration on the operation Hall Thruster Bustlab Hollow Cathode, 52<sup>nd</sup> AIAA/SAE/ASEE Joint Prop. Conf. AIAA 2016-4834 (2016).
5. R. W. Conversano, Low-Power Magnetically Shielded Hall Thrusters, PhD Thesis, University of California. (2015).
6. D. M. Goebel, I. Katz, Fundamentals of Electrical Propulsion, John Wiley. (2008).
7. R. W. Conversano, R. B. Lobbia, K. C. Tilley, D. M. Goebel, S. W. Reilly, I. G. Mikellides, R. R. Hofer, Development and Initial Performance Testing of a LowPower Magnetically Shielded Hall Thruster with an Internally-Mounted Hollow Cathode, 35<sup>th</sup> Int. Elec. Prop. Conf. IEPC-2017-64 (2017).
8. A. A. Martins, M. C. F. Porto, H. O. Coelho, J. L. Ferreira, I. S. Ferreira, Preliminary experimental results of the PHALL II-C with improved magnetic circuit design and hollow cathode, *J. Phys.: Conf. Ser.* 1365 012025 (2019).
9. R. A. Miranda, A. A. Martins, J. L. Ferreira, Particle-in-cell numerical simulations of a cylindrical Hall thruster with permanent magnets, *J. Phys.: Conf. Ser.* 911 02021 (2017).
10. L. Grimaud, S. Mazouffre, Ion behavior in low-power magnetically shielded and unshielded Hall thrusters, *Plasma Sources Sci. Technol.* 26 (2017) 055020.
11. M. C. Porto, A. A. Martins, J. L. Ferreira, C. H. Llanos, Comparative analysis of simulation and experiment for the Hall-type thruster BPT-4000, *Results in Engineering*, 17 (2023) 101006.
12. R. W. Conversano, D. M. Goebel, R. R. Hofer, T. S. Matlock, R. E. Wirz Magnetically Shielded Miniature Hall Thruster: Development and Initial Testing, 33<sup>rd</sup> Int. Elec. Prop. Conf. IEPC-2013-201 (2013).
13. R. A. Martinez, H. Dao, M. L. R. Walker, Power deposition into the discharge channel of a hall effect thruster, *Journal of Propulsion and Power.* (2014) Vol. 30, No. 1, 209220, DOI: 10.2514/1.B34897.
14. L. Grimaud, S. Mazouffre, Performance comparison between standard and magnetically shielded 200 W Hall thrusters with BN-SiO<sub>2</sub> and graphite channel walls, 35<sup>th</sup> Int. Elec. Prop. Conf. IEPC-2017-127 (2017).
15. L. Grimaud, S. Mazouffre, Conducting wall Hall thrusters in magnetic shielding and standard configurations, *Journal of Applied Physics* 122, 033305 (2017).
16. S. Mazouffre, L. Grimaud, S. Tsikata, K. Matyash, R. Scheinder, Investigation of rotating spoke instabilities in a wall-less Hall thruster. Part I: Experiments, 35<sup>th</sup> Int. Elec. Prop. Conf. IEPC-2017-248 (2017).

17. A. Spethmann, T. Trottenberg, H. Kersten, F. G. Hey, L. Grimaud, S. Mazouffre, Application of force measuring probes for the investigation of sputtering and as diagnostic for HEMP and Hall thrusters, 35<sup>th</sup> Int. Elec. Prop. Conf. IEPC-2017-245 (2017).
18. L. Yan, P. Wang, H. Ouyang, X Kang. Thermal analysis of the Hall Thruster in vacuum, Vacuum. (2014) Vol. 108, 40-55.
19. R. A. Martinez, M. R. L. Walker, Propellant thermal management effect on neutral residence time in low-voltage Hall thrusters, Journal of Propulsion and Power. (2013) Vol. 29, No. 3 528-539, DOI: 10.2514/1.B34702.
20. Dassault Systemes, Theoretical Manual for SolidWorks. (2017).

*This page is intentionally left blank*



Scan to know paper details and  
author's profile

# The Usage of Wireless Intelligent Control and UAV-Enabled B5G/6G Network in Fuzzy Adaptive Kalman Filter in INS/GNS Integrated Navigation System

Guangchen Xu & Zhenliang Yu

## ABSTRACT

In the Inertial Navigation System/Geomagnetic Navigation System (INS/GNS) integrated navigation system, divergence and measurement noise that change with environments frequently occur must be reduced so as to extend the accuracy and stability of autonomous, passive navigation. Base on the Unscented Kalman Filter, we can combine Convergence of intelligent sensing as well as computing, and control for UAV-enabled B5G/6G network to deal with change in the variance and mean value of the latest information. First, the noise's covariance in the model is modified "online" to change the estimation of mean square deviation error and filtering gain of Kalman filtering by using 5G/6G network; Then, through UAV-enabled B5G/6G network and intelligent sensing to change the scaling factor of weight in sigma sampling is adaptively changed to solve the nonlocal effect in UT transform and improve the efficiency and accuracy of the navigation deposition system. The simulation findings reveal that the fuzzy adaptive Kalman filter is very efficient for INS/GNS integrated navigation systems. It overcome the short comings of traditional filtering method and improve rove the accuracy of filtering.

**Keywords:** fuzzy adaptive; integrated navigation; scaling factor; unscented kalman filter; ut transform; B5G/6G.

**Classification:** LCC Code: QA75.5-QA76.95

**Language:** English



Great Britain  
Journals Press

LJP Copyright ID: 392923

Print ISSN: 2631-8474

Online ISSN: 2631-8482

London Journal of Engineering Research

Volume 23 | Issue 5 | Compilation 1.0



© 2023, Guangchen Xu & Zhenliang Yu. This is a research/review paper, distributed under the terms of the Creative Commons Attribution-Noncom-mercial 4.0 Unported License (<http://creativecommons.org/licenses/by-nc/4.0/>), permitting all noncommercial use, distribution, and reproduction in any medium, provided the original work is properly cited.



# The Usage of Wireless Intelligent Control and UAV-Enabled B5G/6G Network in Fuzzy Adaptive Kalman Filter in INS/GNS Integrated Navigation System

Guangchen Xu<sup>a</sup> & Zhenliang Yu<sup>o</sup>

## ABSTRACT

*In the Inertial Navigation System/Geomagnetic Navigation System (INS/GNS) integrated navigation system, divergence and measurement noise that change with environments frequently occur must be reduced so as to extend the accuracy and stability of autonomous, passive navigation. Base on the Unscented Kalman Filter, we can combine Convergence of intelligent sensing as well as computing, and control for UAV-enabled B5G/6G network to deal with change in the variance and mean value of the latest information. First, the noise's covariance in the model is modified "online" to change the estimation of mean square deviation error and filtering gain of Kalman filtering by using 5G/6G network; Then, through UAV-enabled B5G/6G network and intelligent sensing to change the scaling factor of weight in sigma sampling is adaptively changed to solve the nonlocal effect in UT transform and improve the efficiency and accuracy of the navigation deposition system. The simulation findings reveal that the fuzzy adaptive Kalman filter is very efficient for INS/GNS integrated navigation systems. It overcome the short comings of traditional filtering method and improve rove the accuracy of filtering.*

**Keywords:** fuzzy adaptive; integrated navigation; scaling factor; unscented kalman filter; ut transform; B5G/6G.

**Author** <sup>a</sup> <sup>o</sup>: Mechanical and Power Engineering College, Yingkou Institute of Technology, Yingkou, China.

## I. INTRODUCTION

The fundamental physical field of the Earth is the geomagnetic field. Any location in the vicinity of Earth has a magnetic field, and the strength and direction of the field depend on the location's longitude, latitude, and altitude. The geomagnetic field has abundant parameter information, such as the total geomagnetic field, the three-component geomagnetism, the inclination angle, the declination angle and the geomagnetic field gradient. This provides sufficient matching information for the geomagnetic navigation algorithm. Geomagnetic navigation does not need to receive external information and belongs to both active and passive navigation. The long-term stability of geomagnetic matching technology can make up for the deficiencies of the inertial navigation system's long-term faults if inertial navigation and geomagnetic matching technology are combined. Additionally, the geomagnetic matching system's vulnerability to interference can be offset by the inertial navigation system's short-term high precision. Inertial/geomagnetic integrated navigation can be applied to the autonomous navigation of submarines, ships, vehicles and other carriers as well as long-range weapons such as missiles. It has shown important military value and promising application prospects.

At present, geomagnetic navigation algorithms include the theory of maximum correlation, ICCP algorithm [1], neural networks and statistical pattern recognition algorithms, the most widely used of which is the extended Kalman filter (EKF) [2] method. In this method, the nonlinear system is linearized by the Taylor expansion method, and

the linear transformation in the Kalman equation is replaced by the Jacobian matrix. Although EKF maintains the advantages of Kalman filtering and effective iterative updates in calculations, it essentially approximates linearization of nonlinear models. For strong nonlinear problems or when the Jacobian matrix is unavailable, the EKF cannot obtain satisfactory results [3].

Therefore, Julier and Uhlmann [4] put forward the Unscented Kalman Filter (UKF) method based on the idea of multiple function representative points, which overcomes the above shortcomings of EKF. However, in the practical application of UKF, obtaining statistical knowledge of system noise and observation noise is difficult. In general, the process noise, measurement noise and innovation are no longer white noise processes. In this case, traditional Kalman Filters can easily cause filtering to diverge. In this study, an adaptive Kalman filter is used to reduce the impact of unusual measurement data and produce precise system state estimate. The scaling factor  $\alpha$  of the noise variance matrix in the model and the weight in the sigma sampling "on-line" can be changed to alter the estimated filter gain matrix and mean square error matrix.

## II. METHODOLOGY

### 2.1 UT Transformation

The UT transformation serves as the cornerstone of UKF. The Unscented Transformation (UT) does not require linearization of the nonlinear system since a nonlinear probability distribution can be approximated more easily than any nonlinear function. Instead, it uses a certain sampling approach to choose a predetermined number of sigma sampling points. These sampling points have the same mean  $\bar{x}$  and covariance  $P_{xx}$  as the system state distribution. After nonlinear transformation, these sigma sampling points can approach the posterior mean  $\bar{y}$  and covariance  $P_{yy}$  with second-order accuracy. Applying the UT transform to the Kalman filter results in the UKF is formed. The following is the UT transformation process [5]:

$$\{\chi_i\} = [\bar{x} \quad \bar{x} + \sqrt{(L+\lambda) P_{xx}} \quad \bar{x} - \sqrt{(L+\lambda) P_{xx}}] \tag{3}$$

According to the  $x$  statistics  $\bar{x}$  and  $P_{xx}$  of the input variables, select a sigma point sampling strategy to obtain the sigma point set  $\{\chi_i\}$ ,  $i=1, \dots, L$  of the input variable and the corresponding weights  $W_i^m$  and  $W_i^c$ , where  $L$  is the number of sampling points used in the sampling strategy; The weights used for mean and covariance weighting are  $W_i^m$  and  $W_i^c$ , respectively.

Perform a nonlinear transformation on each sampling point in the sampled input variable sigma point set  $\{\chi_i\}$  to obtain the transformed sigma point set  $\{y_i\}$ ,  $y_i = f(x_i), i=1, \dots, L$ .

By weighting the sigma point set  $\{y_i\}$  after nonlinear transformation, the statistics  $\bar{y}$  and  $P_{yy}$  of the output variable  $y$  are obtained.

$$\bar{y} = \sum_{i=0}^{L-1} W_i^m y_i \tag{1}$$

$$P_{yy} = \sum_{i=0}^{L-1} W_i^c (y_i - \bar{y})(y_i - \bar{y})^T \tag{2}$$

### 2.2 Proportional Revision

The minimal skew simplex sampling is a strategy to minimize the number of sampling points. It minimizes the skewness (the third-order moment) on the premise that the sampling point set captures the first two order moments of the random variable  $x$ . In the minimum skewness simplex sampling strategy, the sampling points are not centrosymmetric. The nonlocal effect problem is caused by the fact that as the dimension grows, the distance from the sample point extending from the low dimension to the center point grows. Julier et al. proposed a proportional UT transform in which the sampling strategy in the general UT transform is proportionally modified [6]. This transformation can solve the problem of non-local effects by adjusting the value of the parameter  $\alpha$ . The specific sigma point sampling rule is as follows:



$$W_i^m = \begin{cases} \lambda / (L + \lambda), i = 0 \\ 1 / 2(L + \lambda), i \neq 0 \end{cases} \quad (4)$$

$$W_i^c = \begin{cases} \lambda / (L + \lambda) + (1 - \alpha^2 + \beta), i = 0 \\ 1 / 2(L + \lambda), i \neq 0 \end{cases} \quad (5)$$

Where  $\lambda = \alpha^2(L + \kappa) - L$ . Let be  $\kappa \geq 0$  to ensure that the variance matrix is semidefinite,  $\kappa$  generally defaults to 0 or  $3 - L$ . The scope of  $L$  is  $0 < L < 3$ .  $W_i^c$  and  $W_i^m$  are the weights used in the covariance and mean weighting of UT transform, respectively.  $\alpha$  and  $\beta$  are parameters for the Gaussian distribution,  $\beta = 2$  is optimal [7]. The distance between the sigma point and the center point  $\bar{x}$  is managed by the scale factor  $\alpha$ . It is a relatively small positive number, which is usually taken in the interval  $[10^{-4} \sim 1]$ .

### 2.3 The Selection of Adaptive Scale Factor $\alpha$

The flow of the UKF algorithm can be seen in Figure 1. The UKF filter value  $\hat{X}_k$  at time  $k$  is taken as the center point of the sigma point set generated in the next time prediction, and the other sampling points are distributed near the center point. The covariance  $P_k$  matrix obtained by

the  $k$ -step filtering describes the relationship between the filter value  $\hat{X}_k$  and the real value  $X_k$ , namely:

$$P_k = E[(X_k - \hat{X}_k)(X_k - \hat{X}_k)^T] \quad (6)$$

Therefore, the distance  $d_k$  between the center point and the sigma point set can be approximately calculated by  $P_k$ , namely:

$$d_k \approx \sqrt{\text{tr}(P_k)} \quad (7)$$

The  $k$ -step filter value "approximately covers" the critical region  $O(\hat{X}_k, d_k)$  of the true value, as the sampling range of the sigma sampling point in step  $k+1$ , calculates  $d_{k+1} \approx \sqrt{\text{tr}(P_{k+1})}$ , and obtains the adaptive adjustment measurement sigma sampling of scale factor  $\alpha_{k+1|k}$  [8].

$$\alpha_{k+1|k} = d_k / d_{k+1} \quad (8)$$

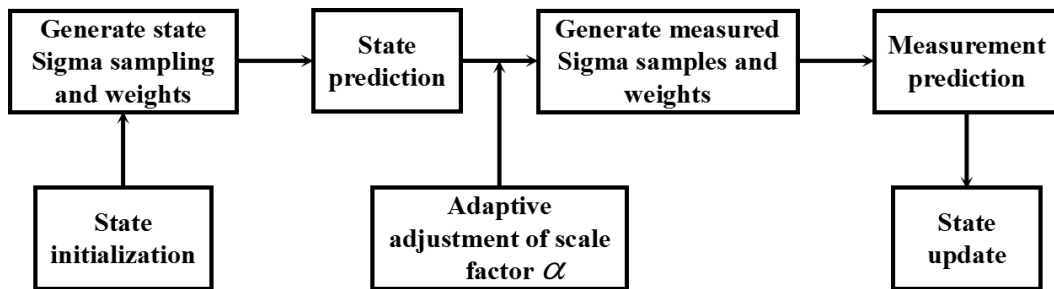


Figure 1: The flowchart of the Proportional Revision UKF Algorithm

### 2.4 Adaptive Control

The residual sequence in the Kalman filter should be white noise with a zero mean if the mathematical model is accurate enough. The Kalman filter's theoretical residual variance should be close to 1 when compared to the measured residual variance. Long-term deviations in the ratio show that the measurement noise level has changed, necessitating an adjustment to the noise covariance matrix sum [9]. To get the ratio back to close to 1, that is the standard for adjustment.

Let's set the model's noise variance matrix to:

$$\begin{cases} Q_k = \gamma Q \\ R_k = \gamma R \end{cases} \quad (9)$$

Where:  $Q$  is the system noise variance matrix,  $R$  is the measurement noise variance matrix.

Matrices  $Q$  and  $R$  are fixed values; The adjustment value  $\gamma$ , modifies the measurement noise variance matrix and the system noise in an adaptive manner. The fuzzy adaptive Kalman filter is developed as follows to put the aforementioned idea into practice.

*In the formula:* the matrix sum is a fixed value. An adjustment value, adaptively adjusts the system noise and measures the noise variance matrix. The concepts discussed above are used to design the fuzzy adaptive Kalman filter[10].

The one-step prediction of the state estimate is:

$$\hat{X}_{k|k-1} = \Phi_{k,k-1} \hat{X}_{k-1} \quad (10)$$

The n-dimensional state one-step transition matrix  $\Phi_{k,k-1}$  is used in the equation.

The mean square error matrix of the one-step forecast is:

$$P_{k|k-1} = \Phi_{k,k-1} P_{k-1} \Phi_{k,k-1}^T + \gamma_k Q \quad (11)$$

The Kalman filter's gain matrix is:

$$K_k = P_{k|k-1} H_k^T (H_k P_{k|k-1} H_k^T + \gamma_k R)^{-1} \quad (12)$$

The measured value's one-step prediction is:

$$\hat{Z}_k = H_k \hat{X}_{k|k-1} \quad (13)$$

Then, the estimated modified state is:

$$\hat{X}_k = \hat{X}_{k|k-1} + K_k (Z_k - \hat{Z}_k) \quad (14)$$

In addition to least, the matrix of posterior mean square errors is:

$$P_k = (I - K_k H_k) P_{k|k-1} \quad (15)$$

The  $r = Z_k - \hat{Z}_k$ , also known as residual or innovation, measures how dependent the system model is on the measured values. Where,  $I$  represents the identity matrix, whose dimension is the same as the system status quantity [11].

### 2.5 The Fuzzy Adjustment

Fuzzification, the creation of fuzzy control rules, and defuzzification are the three steps in the fuzzy calculation process. The output fuzzy quantity is produced by the fuzzy control rules by inferring from the input fuzzy quantity. The input exact quantity is converted to the input fuzzy quantity using fuzzification. [12]. The output fuzzy quantity is converted into the precise quantity output during the final defuzzification procedure.

The mean value  $\bar{r}$  and variance  $\hat{P}_r$  of the innovation are the inputs to the fuzzy adaptive logic system employed in this study, and the

output is a weighted index that is used to modify the noise variance matrix in the system model.

Ideally, the innovation is zero-mean white noise. If the innovation is not zero-mean white noise in the process of system operation, it indicates that there is a problem with the filter. Assuming that it represents statistics  $n$  over a period of time, the mean and variance of innovation are:

$$\bar{r} = \frac{1}{n} \sum_{j=t-L}^t r_j \quad (16)$$

$$\hat{P}_r = \frac{1}{n} \sum_{j=t-L+1}^t r_j r_j^T \quad (17)$$

Compare the theoretical value of the variance to the estimated value of the variance. When the estimated value becomes larger than the theoretical value and the mean value gradually moves away from the zero point, it indicates that the filter becomes more and more unstable. At this moment, adjusting the noise intensity is required to enhance the filter's performance.

The mean and variance are determined by keeping track of the innovation at each filter sample point. If the variance of innovation increases and the mean value approaches zero, the system noise should be reduced while the measurement noise should be increased to obtain a smaller  $\gamma$  value. As a result, the gain matrix of the filter will diminish the system's trust and use of the measured value and the filtering performance tends to become more stable.

The innovation variance and mean value are divided into three levels as fuzzy input: Zero, Small, and Large; The output  $\gamma$  is divided into four levels: Zero, Small, Medium, and Large; The common method of generating fuzzy control rules is through expert experience, expressed in the form shown in Table 1.

Table 1: Rules for fuzzy inference

$\gamma$		Mean $\bar{r}$		
		Zero	Small	Large
Variance $\hat{P}_r$	Zero	Large	Zero	Large
	Small	Zero	Large	Medium
	Large	Large	Medium	Zero

2.6 The Proportional Minimum Skewness UKF Algorithm of Fuzzy Adaptive

Following linearization, the discrete system's mathematical model looks like this:

$$\begin{cases} X_k = \Phi_{k,k-1} X_{k-1} + \omega_k \\ Z_k = H_k X_k + v_k \end{cases} \quad (18)$$

$X_k$ ,  $Z_k$ , and  $H_k$  represent the system state vector, measurement vector, and measurement matrix, respectively. The system noise vector  $\omega_k$  is white noise, namely:  $\omega_k \sim N(0, Q)$ ,  $Q$  is the system noise variance matrix; The measurement noise vector  $v_k$  is also white noise, namely:  $v_k \sim N(0, R)$ ,  $R$  is the measurement noise variance matrix.

$$P_{k+1|k} = \sum_{i=0}^{L-1} W_i^c [(\chi_{k+1|k}(i) - \hat{X}_{k+1|k})][(\chi_{k+1|k}(i) - \hat{X}_{k+1|k})]^T + \gamma_k Q \quad (20)$$

Measure sigma sampling, use  $\hat{X}_{k+1|k}$  and  $P_{k+1|k}$  to regenerate the sampling point set and weight  $\{\chi_{k+1|k}(i), W_i^m, W_i^c\}$ .

$$y_{k+1|k}(i) = h[\chi_{k+1|k}(i), u] \quad (21)$$

The prediction, variance and covariance are respectively:

$$\hat{Z}_{k+1|k} = \sum_{i=0}^{L-1} W_i^m y_{k+1|k}(i) \quad (22)$$

$$P_{ZZ} = \sum_{i=0}^{L-1} W_i^c [(y_{k+1|k}(i) - \hat{Z}_{k+1|k})][(y_{k+1|k}(i) - \hat{Z}_{k+1|k})]^T + \gamma_k R \quad (23)$$

$$P_{XZ} = \sum_{i=0}^{L-1} W_i^c [(y_{k+1|k}(i) - \hat{Z}_{k+1|k})][(y_{k+1|k}(i) - \hat{X}_{k+1|k})]^T \quad (24)$$

Update the state and variance, and calculate the filter gain.

$$W_{k+1} = P_{XZ} P_{ZZ}^{-1} \quad (25)$$

$$\hat{X}_{k+1} = \hat{X}_{k+1|k} + W_{k+1} (Z_{k+1} - \hat{Z}_{k+1|k}) \quad (26)$$

$$P_{k+1} = P_{k+1|k} - W_{k+1} P_{ZZ} W_{k+1}^{-1} \quad (27)$$

Here is the specific UKF algorithm:

The state initialization given  $\hat{X}_0 = E(X_0)$ ,  $P_0 = E[(X_0 - \hat{X}_0)(X_0 - \hat{X}_0)^T]$ .

Select sampling points and weights:  $\{\chi_k(i), W_i^m, W_i^c\}$ .

The nonlinear system model  $\chi_{k+1|k}(i) = f(\chi_i, u)$  computes the mean and covariance of the predicted state:

$$\hat{X}_{k+1|k} = \sum_{i=0}^{L-1} W_i^m \chi_{k+1|k}(i) \quad (19)$$

The fuzzy adaptive unscented Kalman filter is shown in Figure 2.

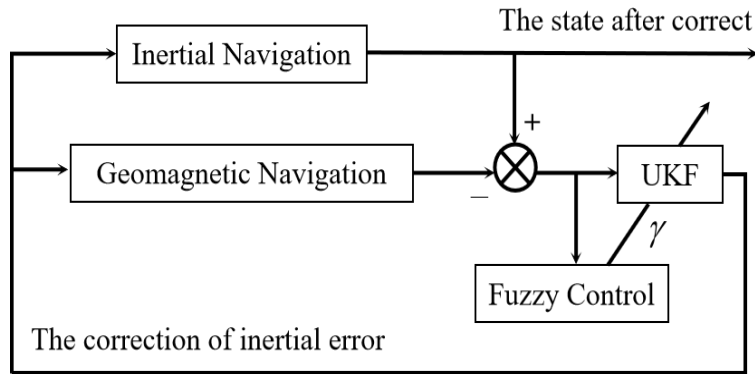


Figure 2: The Fuzzy Adaptive unscented Kalman Filter

### III. SIMULATION AND DISCUSSION

The initial simulation conditions are as follows: The gyro drift is 0.01 (.) /h; The root mean square of gyro drift white noise is 0.01(.) /h; The initial position of the system is  $X_0 = [50, 30, 0.35, 0.35]^T$ ; The

initial variance matrix of the system  $P_0 = \begin{bmatrix} 0.1 & 0 & 0 & 0 \\ 0 & 0.1 & 0 & 0 \\ 0 & 0 & 0.1 & 0 \\ 0 & 0 & 0 & 0.1 \end{bmatrix}$  is a diagonal matrix; The variance matrices

for the system's state noise and measurement noise are  $Q = \begin{bmatrix} 0.05 & 0 & 0 & 0 \\ 0 & 0.05 & 0 & 0 \\ 0 & 0 & 0.001 & 0 \\ 0 & 0 & 0 & 0.001 \end{bmatrix}$  and  $R = \begin{bmatrix} 1 & 0 \\ 0 & 0.001 \end{bmatrix}$ ,

respectively. In the MATLAB R2018 environment, the simulation time of Monte Carlo is 100s. The simulation results are as follows:

Table 2: Filter Performance Comparison

Filter	RMS (errors)	Time (s)
EKF	0.12863	0.08362
UKF	0.11953	0.26742
FUKF	0.11176	0.47879

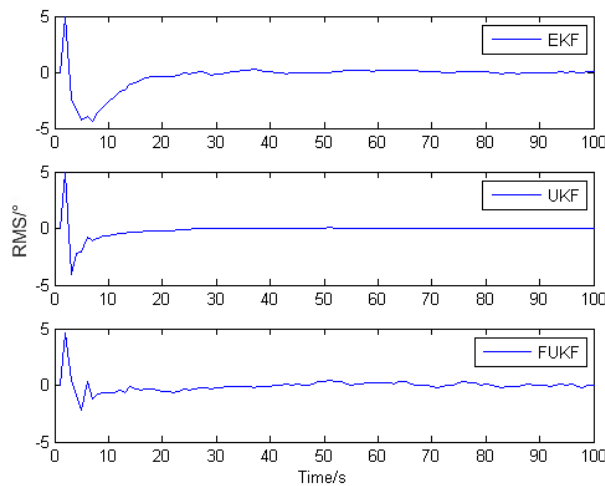


Figure 3: The curve of RMS error

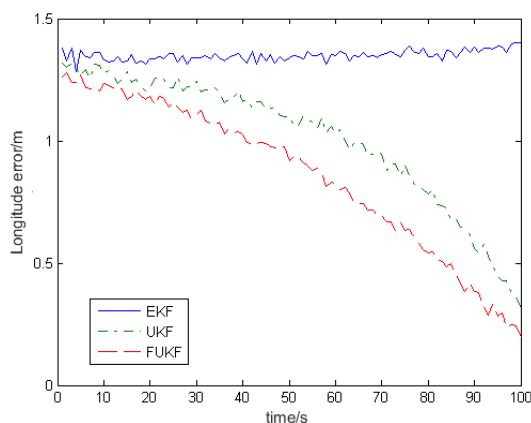


Figure 4: The Curve of Longitude Error

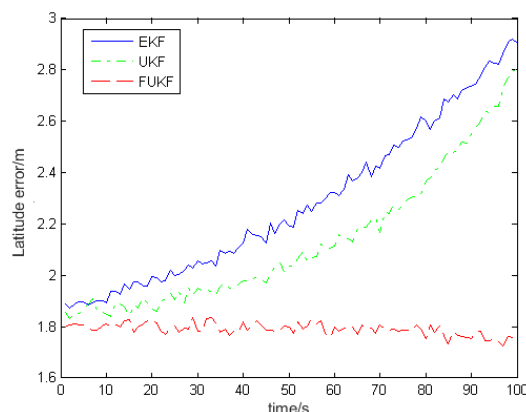


Figure 5: The Curve of Latitude Error

It can be seen from Table 2 that compared with the EKF and UKF filtering algorithms, the fuzzy adaptive filtering algorithm has a smaller filtering error and larger calculation amount, resulting in increased calculation time.

Figure 3 shows that the FUKF filtering algorithm has fast convergence and a minimal filtering error. The Figures 4 and 5 show that the FUKF filtering algorithm can effectively suppress filtering divergence, with stable performance, and further improve the filtering effect of navigation system. In 100s, the system error remains within the range of the navigation accuracy. It is obvious that the model error can be successfully reduced by using the time-varying noise statistical estimator to estimate and correct the statistical features of system noise and observation noise in real time.

#### IV. CONCLUSION

The fuzzy adaptive unscented Kalman filtering approach suggested in this article modifies the

model's noise variance matrix "online" in order to update the estimated mean square error and filtering gain. Additionally, it can handle the non-local impacts of UT transformation by adaptively adjusting the scaling factor of the weights in sigma sampling. The results show that the fuzzy adaptive Kalman filter is suitable for the inertial/geomagnetic integrated navigation system, and the measurement noise of the model is adaptive. When the nonlinearity is severe, this can effectively solve the issue of filtering divergence in the integrated navigation system.

#### ACKNOWLEDGEMENTS

The authors acknowledge the Natural Science Foundation of Liaoning (Grant: 2021-YKLH-03).

#### Data sharing agreement

The corresponding author will provide the datasets used and/or analyzed during the current work upon reasonable request.

### Declaration of Conflicting Interests

The author certifies that there are no possible conflicts of interest in this article's research, writing, and/or publishing.

### REFERENCES

1. Yingjing. Guo, Fang. Kong, Manlin. Zhang and Wenhong. Lyu (2020) Review of integrated navigation system for AUV, Navigation Positioning. Timing., 7 (5): 107–119.
2. Wenxuan. Fang, Dianwei. Cong (2022) Status and development of multi-source information fusion technology for satellite/Inertial/visual integrated navigation, Radio Engineering., 52 (10): 1813-1820.
3. Yixian. Zhu, Ling. Zhou (2021) Fuzzy Adaptive Filtering Algorithm Used in Autonomous Underwater Vehicle Integrated Navigation System, Journal of Nantong University., 20 (1): 34–39.
4. Julier S.Uhlmann, Durrant W H F (2020) A New Method for the Nonlinear Transformation of Means and Covariance in Filters and Estimators, IEEE Transacts on Automatic Control., 45 (3): 477-482.
5. Qiang. Fu, Hongyue. Zhao, Xiyun. Sun and Yuanfa. Ji (2020) Application research of improved strong tracking UKF algorithm in integrated navigation, Computer Simulation., 38 (2): 29-33.
6. Ping. Huang, Ting. Sun, Yanlong. Tong (2018) UKF integrated navigation algorithm based on adaptive simplex sampling, Systems Engineering and Electronics., 40 (7): 1567- 1572.
7. Haykin S (2002) Kalman Filtering and neural networks, John Wiley & Sons Inc.
8. Luying. Zhu, Weiwei. Sun, Chengming. Liu and Zhaowei. Sun (2022) Research on federal UKF algorithm for multi-sensor integrated navigation system, Journal of Electronic Measurement and Instrumentation., 36 (7): 91-98.
9. Xiaojie. Ma, Xueyuan. Lin, Qiaoyan. Sun and Xiangguang. Chen (2021) Improved UKF algorithm for BDS/SINS integrated navigation system, Journal of Geodesy and Geodynamics., 41 (4): 351-356.
10. Wangyan. Qiu, Rongbing. Li, Jianye. Liu (2020) Research on GNSS/MINS integrated navigation algorithm of general aviation based on improved adaptive fading kalman filter, Electronic Measurement Technology., 43 (10): 95-100.
11. Mehrnaz Poostpasand. Reza Javidan (2018) An adaptive target tracking method for 3D underwater wireless sensor networks, Wireless Networks., 24: 2797-2810.
12. Xiaobin. Xu, Minzhou. Luo, Zhiying. Tan and Min. Zhang (2019) Measured accuracy improvement method of velocity and displacement based on adaptive Kalman filter, Sensor Review., 39 (5): 708-715.



Scan to know paper details and  
author's profile

# A Study on the Possibility of Utilizing Coffee Waste as a Recycled Resource Material using Ultrasonic Extraction Method

Taeyeob Lee, Yuri Kang & Woonjung Kim

University of Hannam

## ABSTRACT

In this study, in order to confirm the potential of coffee waste as a recyclable resource material, the caffeine content of coffee waste and the effective active ingredients of coffee waste extract were confirmed using an ultrasonic extraction method. In order to conduct a preliminary experiment to determine whether extraction of coffee waste affects caffeine reduction, ultrasonic extraction was performed after immersion at room temperature for 48 hours at ethanol content of 0%, 30%, 50%, 70%, and 100%. The coffee waste recovered after extraction were analyzed for active ingredients using GC-MS.

Except for the coffee waste after extraction with 100% ethanol, almost no components other than caffeine were detected in the coffee waste recovered after extraction by ethanol content. As a result of quantitative analysis of caffeine in coffee grounds using LC-MS, a caffeine reduction rate of 72.1% was confirmed in the coffee grounds recovered after ultrasonic extraction with 70% ethanol.

*Keywords:* coffee waste, recycle, caffeine, ultrasonic extraction, decaffeination.

*Classification:* DDC Code: 663.4

*Language:* English



Great Britain  
Journals Press

LJP Copyright ID: 392924

Print ISSN: 2631-8474

Online ISSN: 2631-8482

London Journal of Engineering Research

Volume 23 | Issue 5 | Compilation 1.0







# A Study on the Possibility of Utilizing Coffee Waste as a Recycled Resource Material Using Ultrasonic Extraction Method

Taeyeob Lee<sup>a</sup>, Yuri Kang<sup>o</sup> & Woonjung Kim<sup>p</sup>

## ABSTRACT

*In this study, to confirm the potential of coffee waste as a recyclable resource material, the caffeine content of coffee waste and the effective active ingredients of coffee waste extract were established using an ultrasonic extraction method. To conduct a preliminary experiment to determine whether extraction of coffee waste affects caffeine reduction, ultrasonic extraction was performed after immersion at room temperature for 48 hours at ethanol content of 0%, 30%, 50%, 70%, and 100%. The coffee waste recovered after extraction was analyzed for active ingredients using GC-MS. Except for the coffee waste after extraction with 100% ethanol, almost no components other than caffeine were detected in the coffee waste recovered after extraction by ethanol content. As a result of quantitative analysis of caffeine in coffee grounds using LC-MS, a caffeine removal rate of 72.1% was confirmed in the coffee grounds recovered after ultrasonic extraction with 70% ethanol.*

*As a result of a preliminary experimental study, this study was conducted to confirm whether repeated re-extraction removed more than 90% of the caffeine content in the coffee waste and met the decaffeination standard. Based on the results of a preliminary experiment that confirmed the highest caffeine reduction rate in ultrasonic extracted coffee waste with 70% ethanol content, extraction was repeated 1 to 3 times using coffee waste with 70% ethanol content in the same manner as the preliminary experiment. As a result of quantitative analysis of caffeine in coffee waste using LC-MS in this experiment, a high reduction rate of 99.5% of caffeine content was confirmed to be removed from coffee waste*

*recovered by repeated extraction with 70% ethanol three times.*

**Keywords:** coffee waste, recycle, caffeine, ultrasonic extraction, decaffeination.

**Author  $\alpha$   $\sigma$ :** Department of Cosmetic science, University of Hannam, Daejeon, 34430, Korea.

**p:** Department of Chemistry, University of Hannam, Daejeon, 34430, Korea.

## I. INTRODUCTION

The development of the food industry and food processing technology, along with the improvement of the standard of living of modern people, has shaped the coffee culture [1, 2, 3]. Coffee has become an essential item in the preferences of contemporary individuals, to the extent that it is often referred to as the "second water"[4]. How to make a cup of Americano, coffee is extracted using water, roasted coffee beans, The seeds of the coffee tree's fruit[5].

During the coffee extraction process, coffee waste, which refers to the leftover residues after the coffee extraction process, is generated. When making a cup of coffee, approximately 15 grams of coffee beans are used, with 14.7 grams being discarded, and 0.3 grams, which is 2%, is consumed as a beverage [6]. Coffee waste is generated worldwide at a rate of 10 million tons annually, and the amount of coffee waste is increasing by coffee consumption. In 2019, an 149,038 tons of coffee waste were produced [7, 8]. If such coffee waste is incinerated or landfilled without recycling, it incurs an annual cost of KRW 35 billion [9, 10].

Decaffeination refers to removing caffeine from coffee beans, cocoa, tea leaves, and other

Decaffeination refers to the process of removing caffeine from coffee beans, cocoa, tea leaves, and other substances that contain caffeine. Therefore, decaffeinated coffee typically contains 1-2% of the original caffeine component, making it suitable for pregnant women, diabetes patients, and individuals with sensitive stomachs, and it is also known as 'caffeine-free' coffee [11]. The international standard for decaffeinated coffee is that more than 97% of caffeine is removed. Therefore, even in decaffeinated coffee, a small amount of caffeine may still be contained [12].

Caffeine is a compound formed by combining 'Coffee' with '-ine,' representing an alkaloid substance that collectively refers to basic organic compounds found within plant organisms. Alkaloid substances often exhibit significant physiological and pharmacological effects, with notable examples including nicotine, morphine, and caffeine. Caffeine has a stimulating effect on the central and the peripheral nervous system, which results in mental alertness and an increase in concentration and productivity [13, 14].

Therefore, caffeine may have some benefits for adults, but its impact on the central nervous system of children has not been sufficiently researched yet. The central nervous system of children is still in development, which raises concerns about the potential side effects and health implications of caffeine [15]. Caffeine can be absorbed through the skin, so caution is necessary when using caffeine-containing substances in items for children, such as educational aids.

Research on the utilization of coffee waste includes studies on artificial cover material manufacturing for sewage sludge using coffee sludge [16], activated carbon adsorbents [17], eco-friendly composting [18], wastewater treatment [19], coffee soap, and air freshener production [20]. However, the actual usage of coffee waste remains minimal. Furthermore, recently, some clay products for children have incorporated recycled materials, including coffee waste. However, existing clay products made with recycled coffee waste have limitations for use by children due to factors such as caffeine content.

Therefore, educational aids made from recycled coffee waste should minimize caffeine content, taking into account the age and sensitivity of children. Therefore, the purpose of this study is to confirm the reduction of caffeine using a repeated extraction method with coffee waste, investigate its decaffeination potential, assess the feasibility of coffee waste as a sustainable resource, and check its safety and potential as a recyclable resource material.

## II. EXPERIMENT

### 2.1 Materials

The coffee waste used in this study were provided by Harmony Co., Ltd. in the form of coffee ground powder in February 2023 and were stored at room temperature for conducting experiments.

### 2.2 Extraction Condition Experiment for Coffee Waste I

For Experiment I of coffee waste extraction, distilled water and ethanol were used as solvents. The volume was set at 300 ml, with a sample weight of 30 g. Ethanol was used in varying concentrations of 0%, 30%, 50%, 70%, and 100%, and extraction was carried out at room temperature for 48 hours after immersion. The ultrasonic extraction conditions involved using an extraction device (ULTRA SONIC, BMWWORKS, Daejeon, Korea) at a temperature of 20°C, operating at 20 kHz for 30 minutes. The extracted solution was subjected to decompressed filtration through a 5-8  $\mu\text{m}$  filter (Hyun Dai, Micro, Korea) using a vacuum pump (DOA-P704-AC, GAST Manufacturing Inc, U.S.A). After the filtration, the coffee extract was dried in a 60°C Coven for 48 hours and stored at 4°C for GC-MS analysis and caffeine analysis.

### 2.3 Repeated Extraction Experimental Conditions for Coffee Waste II

For the repeated extraction of coffee waste in Experiment II, the same solvents, water and ethanol, were used as in Experiment I. For the ultrasonic extraction conditions for Experiment II, the volume was set at 300 ml, with a sample weight of 30 g, and 70% ethanol was used. The extraction was carried out in the same way as

Experiment 1 at room temperature for 48 hours after immersion. After filtration, the coffee waste was dried in a 60°C oven for 48 hours, and the process of obtaining the coffee waste extraction material was repeated 1-3 times.

#### 2.4 Caffeine Quantification in Coffee Waste Using LC-MS

The caffeine content in coffee waste was analyzed using HPLC (Agilent 1290). After a 50 mg sample was measured and injected into a vial, 2 ml of methanol was added, and sonication was carried out for 60 minutes. The analysis was conducted using a 0.45 μm PVDF syringe filter. An LC column, Kinetex 2.6 μm EVO C18 100Å 2.1×100 mm, was used. The column temperature was maintained at 40°C, with a flow rate of 0.300 mL/min, and an injection volume of μl. The MS was conducted under the conditions of a gas temperature of 300°C, a drying gas flow rate of 10 L/min, and a nebulizer pressure of 45 psi. The LC-MS analysis method for this experiment was carried out using in the same way.

#### 2.5 Effective Active Ingredients Analysis in Coffee Waste Extract Using GC-MS

For the analysis of effective active ingredients in the coffee waste extract for Experiment I, GC-MS

(Gas chromatography-mass spectrometry) was used. For the GC analysis, a column (Agilent 19091S-433) was used with HP-5ms (30 m x 250 μm x 0.25 μm), and the analysis was conducted for 45 minutes. The injection volume was μl, and the carrier gas was helium maintained at a flow rate of 10 mL/min. The oven temperature was initially held at 40°C for 3 minutes and then increased at a rate of 5°C/min to a final temperature of 300°C, which was held for 1 minute during the analysis.

### III. RESULTS AND CONSIDERATIONS

The results for the coffee waste recovered after ultrasonic extraction in this study are as follows. The coffee waste recovered after extraction in Experiment I was labeled as original materials (ORG) and A to E, depending on the ethanol content.

The coffee waste recovered after extraction with 0% ethanol ultrasonic extraction is labeled as A, 30% ethanol as B, 50% ethanol as C, 70% ethanol as D, and 100% ethanol as E, as shown in <Table 1>.

*Table 1:* Numbering Based on the Ethanol Content of the Extract by Ultrasonic Extractor

DW : Ethanol	Ultrasonic extractor
100 : 0	A
70 : 30	B
50 : 50	C
30 : 70	D
0 : 100	E

In Experiment II, depending on the number of extractions, the recollected materials were labeled as original materials (ORG) and G1 to G3.

The coffee waste recovered after ultrasonic extraction with 70% ethanol is labeled as G1 for

the first extraction, G2 for the second extraction, and G3 for the third extraction, as shown in <Table 2>.

*Table 2:* Numbering Based on the Ethanol Content of the Extract by Ultrasonic Extractor

DW : Ethanol	Number of Repeated Extractions	Ultrasonic extractor
30 : 70	1 time	G1
	2 times	G2
	3 times	G3

### 3.1. Caffeine Content Analysis of Coffee Waste Using LC-MS

The caffeine content of coffee waste analyzed using LC-MS is as follows.

As shown in <Table 3 & Figure 1>, the 70% ethanol ultrasonic coffee waste exhibited the lowest caffeine content at 404.89 µg/g, showing a 72.1% reduction in caffeine compared to the initial caffeine content of the ORG <Table 4>.

**Table 3:** LC-MS Quantitative Analysis Results for Caffeine in the Coffee Waste Extract by the Ultrasonic Device Used in the Experiment

Sample	mg	g	Caffeine Content in 2 ml of Extracted Methanol (µg)	A 10-Fold Dilution factor	Final Concentration µg/g
ORG	46.9	0.0469	6.809	68.093	1451.9
A	47.4	0.0474	6.676	66.763	1408.5
B	53.4	0.0534	3.976	39.760	744.57
C	50.5	0.0505	3.841	38.411	760.61
D	50.7	0.0507	2.053	20.528	404.89
E	51.3	0.0513	6.650	66.504	1296.4

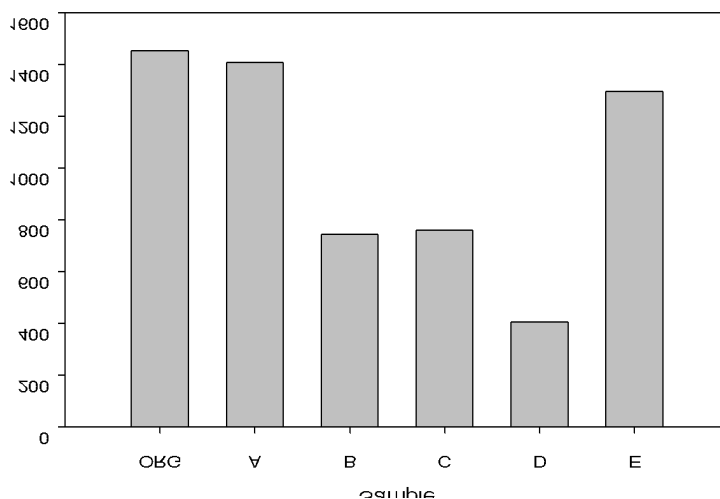


**Figure 1:** Comparison of LC-MS Quantitative Analysis Results of Caffeine in Coffee Waste Extract by Ultrasonic Device Used in the Experiment;

**Table 4:** Final Concentration Reduction Rate as a Result of LC-MS Quantitative Analysis of Caffeine in the Coffee Waste Extract by the Ultrasonic Device Used in the Experiment

Sample	Final Concentration (µg/g)	Reduction Rate (%)
ORG	1451.9	-
A	1408.5	3.00
B	744.57	48.7
C	760.61	47.6
D	404.89	72.1
E	1296.4	10.7

### 3.2 GC-MS Analysis of Effective Active Ingredients in Coffee Waste

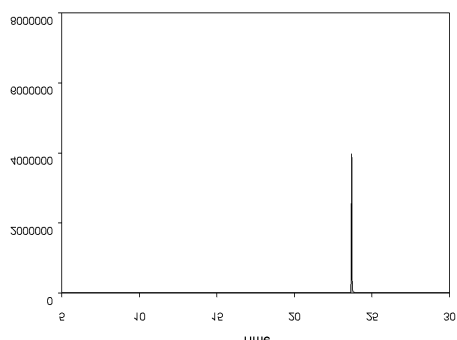
The GC-MS analysis results of effective ingredients in the recovered coffee waste after extraction are presented in <Table 5>. No other compounds were detected in the coffee waste recovered after ultrasonic extraction except for

caffeine. However, in the coffee waste recovered after extraction with 100% ethanol, compounds such as 2,4-Dimethyl-1-heptene, n-hexadecanoic acid, and Benzene were detected. The GC-MS results graph of the coffee waste recovered after extraction, based on the ethanol content, is shown in Figure 2.

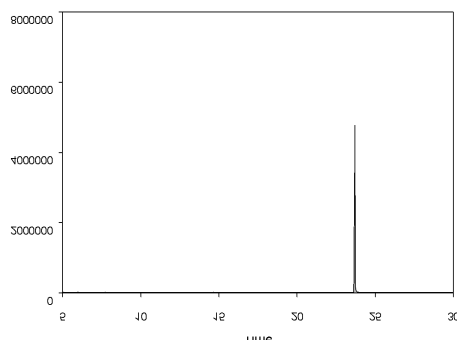
Table 5: Results of GC-MS Analysis of Coffee Waste Extract by Ultrasonic Extractor

(Unit: Area %)

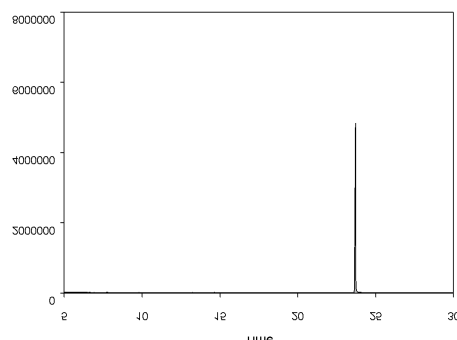
Extract Active Ingredient	Caffeine	2,4-Dimethyl-1-hEptene	n-Hexadecanoicacid (Palmitic Acid)	Benzene
A	100	-	-	-
B	100	-	-	-
C	100	-	-	-
D	17.7	-	-	-
E	19.3	13.4	1.88	10.4



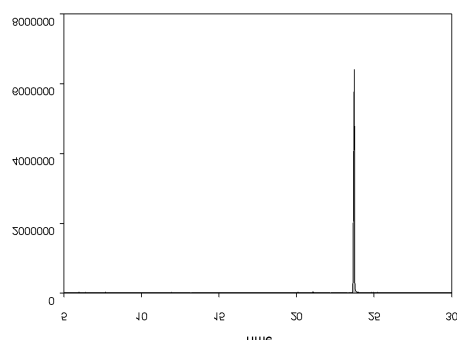
(A)



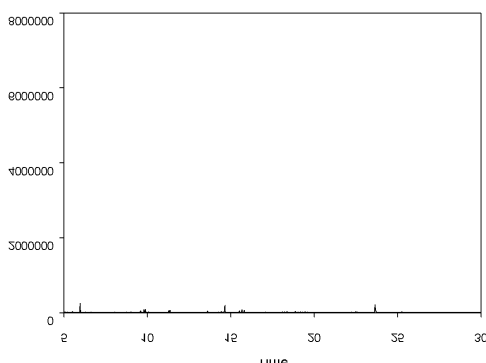
(B)



(C)



(D)



(E)

Figure 2: Comparison of GC-MS Analysis Results of the Coffee Waste Extract by the Ultrasonic Extractor

3.2 Quantitative Analysis Results of Caffeine Using LC-MS for This Experiment

The caffeine content in the coffee waste recovered after ultrasonic extraction is as follows.

As shown in <Table 7 and 8>, a significant caffeine reduction rate of 99.5% was observed in

the coffee waste obtained from ultrasonic extraction using 70% ethanol after three times of repeated extraction. The Korea Food and Drug Administration has confirmed that decaffeination, with 90% removal of caffeine, can be achieved with just two repeated experiments of coffee waste extraction <Figure 3>.

Table 6: LC-MS Quantitative Analysis Results for Caffeine in the Coffee Waste Extract by the Ultrasonic Device Used in the Experiment

Sample	mg	g	Caffeine Content in 2 ml of Extracted Methanol (µg)	A 10-Fold Dilution Factor	Final Concentration µg/g
ORG	53.7	0.0537	12.8	128.1	2386.1
G1	50.0	0.0500	3.22	32.22	644.49
G2	52.0	0.0520	3.55	3.550	68.230
G3	50.6	0.0506	0.59	0.590	11.730

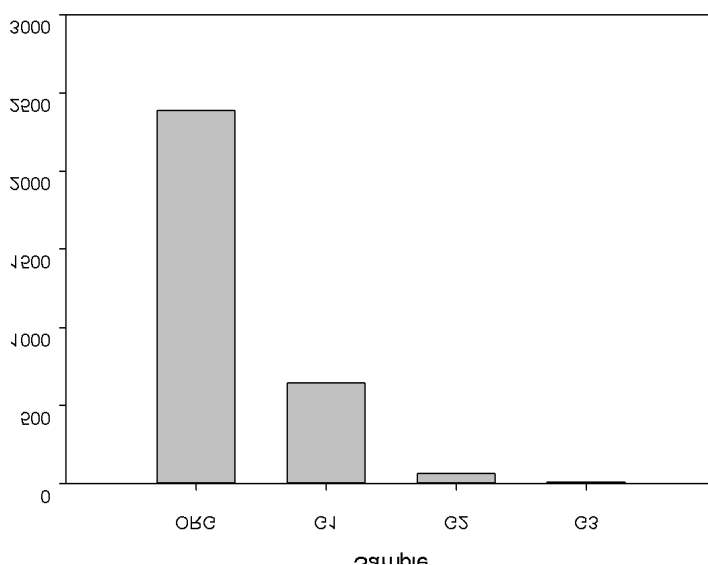


Figure 3: Comparison of LC-MS Quantitative Analysis Results of Caffeine in Coffee Waste Extract by Ultrasonic Device in the Experiment;

**Table 7:** Final Concentration Reduction Rate as a Result of LC-MS Quantitative Analysis of Caffeine in the Coffee Waste Extract by the Ultrasonic Device in the Experiment

Sample	Final Concentration (µg/g)	Reduction Rate (%)
ORG	2386.1	-
G1	644.49	73.0
G2	68.230	97.2
G3	11.730	99.5

## VI. CONCLUSION

This study utilized ultrasonic extraction to investigate the caffeine content and effective active ingredients in coffee waste, confirming its potential as a recyclable resource. The ultrasonic extraction method was used for coffee waste extraction, and preliminary experiments were conducted under conditions ranging from 0% to 100% ethanol content. The GC-MS analysis results of effective ingredients in coffee waste revealed that, except for the coffee waste recovered after 100% ethanol extraction, hardly any other components were detected in coffee waste recovered after extraction with different ethanol contents. The LC-MS analysis of caffeine content revealed a 72.1% reduction in caffeine in the coffee waste recovered after 70% ethanol ultrasonic extraction, compared to the coffee waste without ultrasound extraction.

Furthermore, additional research was conducted to confirm whether the caffeine content within coffee waste could be reduced by over 90% to meet decaffeination standards. The re-extraction was performed using 70% ethanol, which showed the highest caffeine reduction rate among the ethanol concentration ranges. In addition, repeated extraction was performed 1 to 3 times, and the extraction method was ultrasonic extraction conducted under preliminary experimental conditions. The quantitative analysis of caffeine in coffee waste using LC-MS revealed a high caffeine removal rate of 99.5% in the coffee waste recovered after three times repeated extractions with 70% ethanol. As a result of this study, the potential for decaffeination through the repeated ultrasonic extraction of coffee waste was confirmed, and this verified its potential as a recyclable resource material.

## ACKNOWLEDGEMENT

This work was supported by the National Research Foundation of Korea(NRF) grant funded by the Korea government(MSIT) (RS-2023-00281517), and 2023 Local University Revitalization Project funded by the National Research Foundation of Korea.

## REFERENCES

- J. Y. Choi, A Study on Purchasing Characteristics and Consumer Satisfaction on Health Functional Beverage according to Food-related Lifestyle Hotel Resort Research, 12(1), pp.179-196. (2012).
- Scott K, The sweet and the bitter of mammalian taste, *Curr Opin Neurobiol* 14: pp. 423-427, (2004).
- Emile Peynaud, The Taste of wine, The wine appreciation guild, pp. 31-114, 1987.
- H. U. Park, H. E. Lee, World Coffee Industry Trends, *World agriculture*, No. 145, pp. 97-116, (2012).
- Robert HR, Barone J J. Biological effects of caffeine-history and use. *Food Technol*, 37:32-39.(1983).
- S. W. Kim. A Study on the Utilization of Spent Coffee as Animal Feed. Thesis Konkuk University. p11-13. (1990).
- I. C. O (International Coffee Organization) research, Trade Statistics Tables, World coffee consumption. [https://www.ico.org/trade\\_statistics.asp?section=Statistics](https://www.ico.org/trade_statistics.asp?section=Statistics). (2021)
- Y. J. Park, 5 trend changes and prospects in the coffee industry, *Korea Economic Review*, Vol. 848, No. 0, Hyundai Research Institute, 1p, (2019),
- K. M. Kim, Y. S. Park. A plan to turn bio energy into fuel by establishing a coffee grounds collection system. See p.7 (2020).

10. National Assembly Research Service. (Ministry of Foreign Affairs > News, Notices > Press Release, (2021).
11. Zabet GL. Decaffeination using supercritical carbon dioxide. In: Green Sustainable Process for Chemical and Environmental Engineering and Science, Elsevier, Amsterdam, Nederlanden, p 255-278 (2020).
12. KCS (Korea Customs Service). Coffee (bean) import trends in 2022. Available from: <https://www.customs.go.kr/streamdocs/view/sd;stream%20amdocsId=72059269162294321>, Accessed May. 10, (2023).
13. Pohler, H., Caffeine intoxication and addiction, *J. Nurse Pract.*, 6, 49-52, (2010).
14. O'Neil, M. J., *The Merck Index - An encyclopedia of chemicals, drugs, and biologicals*. 14th edition., White house Station, NJ, Merck and Co., Inc, (2013).
15. J. E. Lee, W. Huh, E. J. Choi, Pattern Analysis of High-caffeine Energy Drink Consumption and Adverse Effects among College Students in a University. *Yakhak Hoeji*. 57(2), (2013).
16. G. Y. Lee, H. H. Hyeon, T. J. Ryu, J. Y. Yoon, W. S. Lee, C. H. Lee, K. J. Park, "Re-evaluation of artificial cover for sewage sludge using Busan phosphorus gypsum and coffee sludge". *Journal of the Korean Society of Waste and Resource Circulation* 2011, pp.224-226, (2011).
17. H. Y. Kang, "Adsorption characteristics of activated carbon prepared from coffee grounds", PhD thesis, Chonnam National University Graduate School, (2007).
18. H. S. Kim, "Eco-friendly composting using coffee by-products", master's thesis, Kwangwoon University Graduate School of Environmental Studies, (2012).
19. C. H. Song, C. H. Lee, T. L. Huh, J. H. Ahn, H. C. Yang, Development of substrates for the production of basidiocarps of *Flammulina velutipes*. *Korean J Mycol*.21:212-216, (1993).
20. E. J. Song, J. Y. Kim, S. Y. Lee, S. Y. KIM, K. B. W. R. Kim, S. J. Kim, S. Y. Yoon, S. J. Lee, C. J. Lee, D. H. Ahn, Effect of roasted ground coffee residue extract on shelf-life and quality of salted mackerel. *J Korean SocFood SciNutr*.38:780-786, (2009).



# Great Britain Journal Press Membership

For Authors, subscribers, Boards and organizations



Great Britain Journals Press membership is an elite community of scholars, researchers, scientists, professionals and institutions associated with all the major disciplines. Great Britain memberships are for individuals, research institutions, and universities. Authors, subscribers, Editorial Board members, Advisory Board members, and organizations are all part of member network.

Read more and apply for membership here:  
<https://journalspress.com/journals/membership>



For Authors



For Institutions



For Subscribers

Author Membership provide access to scientific innovation, next generation tools, access to conferences/seminars/symposiums/webinars, networking opportunities, and privileged benefits. Authors may submit research manuscript or paper without being an existing member of GBJP. Once a non-member author submits a research paper he/she becomes a part of "Provisional Author Membership".

Society flourish when two institutions Come together." Organizations, research institutes, and universities can join GBJP Subscription membership or privileged "Fellow Membership" membership facilitating researchers to publish their work with us, become peer reviewers and join us on Advisory Board.

Subscribe to distinguished STM (scientific, technical, and medical) publisher. Subscription membership is available for individuals universities and institutions (print & online). Subscribers can access journals from our libraries, published in different formats like Printed Hardcopy, Interactive PDFs, EPUBs, eBooks, indexable documents and the author managed dynamic live web page articles, LaTeX, PDFs etc.



GO GREEN AND HELP  
SAVE THE ENVIRONMENT

## JOURNAL AVAILABLE IN

PRINTED VERSION, INTERACTIVE PDFS, EPUBS, EBOOKS, INDEXABLE DOCUMENTS AND THE AUTHOR MANAGED DYNAMIC LIVE WEB PAGE ARTICLES, LATEX, PDFS, RESTRUCTURED TEXT, TEXTILE, HTML, DOCBOOK, MEDIAWIKI MARKUP, TWIKI MARKUP, OPML, EMACS ORG-MODE & OTHER



[support@journalspress.com](mailto:support@journalspress.com)  
[www.journalspress.com](http://www.journalspress.com)

 \*THIS JOURNAL SUPPORT AUGMENTED REALITY APPS AND SOFTWARES